Nanostructure-based plasmon-enhanced Raman spectroscopy for surface analysis of materials

Song-Yuan Ding[1], Jun Yi[1], Jian-Feng Li[1,2], Bin Ren[1,2], De-Yin Wu[1], Rajapandiyan Panneerselvam[1] and Zhong-Qun Tian[1]

Abstract | Since 2000, there has been an explosion of activity in the field of plasmon-enhanced Raman spectroscopy (PERS), including surface-enhanced Raman spectroscopy (SERS), tip-enhanced Raman spectroscopy (TERS) and shell-isolated nanoparticle-enhanced Raman spectroscopy (SHINERS). In this Review, we explore the mechanism of PERS and discuss PERS hotspots — nanoscale regions with a strongly enhanced local electromagnetic field — that allow trace-molecule detection, biomolecule analysis and surface characterization of various materials. In particular, we discuss a new generation of hotspots that are generated from hybrid structures combining PERS-active nanostructures and probe materials, which feature a strong local electromagnetic field on the surface of the probe material. Enhancement of surface Raman signals up to five orders of magnitude can be obtained from materials that are weakly SERS active or SERS inactive. We provide a detailed overview of future research directions in the field of PERS, focusing on new PERS-active nanomaterials and nanostructures and the broad application prospect for materials science and technology.

The properties of a surface have crucial roles in determining its adhesion, friction, wear and wetting behaviour, as well as surface chemical processes such as catalysis, corrosion, sintering, composite formation and electrochemistry[1,2]. With the development of surface engineering techniques and nanotechnology, research has shifted from homogeneous to composite materials, from almost perfect single-crystal surfaces to surfaces with functionalized 'active sites', and from thin-film materials to promising 2D materials with one to several atomic layers in thickness. Meanwhile, characterization techniques have been developed to reveal the structure–property relationships of these emerging materials. However, for most techniques, the signals obtained from the surfaces are either too weak to detect or are difficult to resolve into distinct components because of the low spectral and spatial resolution. Therefore, it is necessary to develop *in situ* techniques with ultrahigh sensitivity, surface specificity, high spectral resolution, and high spatial and temporal resolution.

One such technique is surface-enhanced Raman spectroscopy (SERS)[3–5], which can realize an ultrahigh sensitivity down to the single-molecule level by means of coinage-metal (for example, Au, Ag and Cu) nanostructures[6,7]. The SERS effect is due to the amplification of Raman signals of analytes by several orders of magnitude when the analytes are located at or very close to coinage-metal nanostructures (the working principles of SERS are described in BOXES 1,2)[8]. The SERS enhancement of these nanostructures strongly relies on the optical resonance properties of coinage-metal nanostructures, which can significantly enhance the local electromagnetic field, largely owing to the excitation of surface plasmon resonance (SPR)[9,10]. Based on similar surface-enhancement mechanisms, many other surface-enhanced Raman methods, including the two important variants of SERS — tip-enhanced Raman spectroscopy (TERS)[11–14] and shell-isolated nanoparticle-enhanced Raman spectroscopy (SHINERS)[15] — as well as ultraviolet SERS, near-infrared SERS[16–18] and surface-enhanced nonlinear Raman spectroscopy[19–22], have been developed for a wide range of applications. The above-mentioned techniques can be collectively described as plasmon-enhanced Raman spectroscopy (PERS)[23] (a timeline of the key developments of PERS techniques is provided in FIG. 1).

PERS enhancement is strongly dependent on the optical properties, shape and aggregation of nanomaterials[24]. In the 1970s and 1980s, SERS-active substrates, such as roughened Au and Ag electrodes, colloidal aggregates

[1]*State Key Laboratory for Physical Chemistry of Solid Surfaces, College of Chemistry and Chemical Engineering, iChEM, Xiamen University.*
[2]*MOE Key Laboratory of Spectrochemical Analysis and Instrumentation, Xiamen University, Xiamen 361005, China.*

Correspondence to Z.-Q.T.
zqtian@xmu.edu.cn

Article number: 16021
doi:10.1038/natrevmats.2016.21
Published online 26 Apr 2016

Box 1 | **Working principles of SERS**

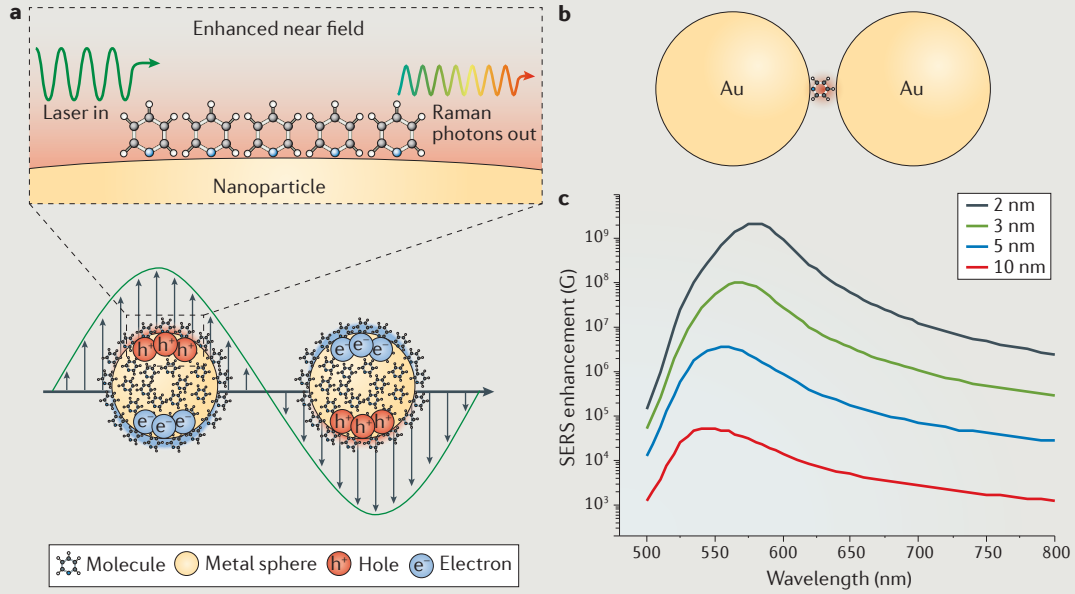

Conduction electrons in metal or metal-like nanomaterials can be coherently excited by incident light to oscillate collectively at metal/dielectric interfaces[154]. The collective oscillating mode of electrons and the nanomaterials that support them are referred to as surface plasmons and plasmonic materials, respectively[123,126]. There are two types of surface plasmons: localized surface plasmons (LSPs), in which coherent electrons oscillate around the nanoparticle surfaces (panel **a**) or nanoscale crevices (panel **b**), and propagating surface plasmons (that is, surface plasmon polaritons (SPPs)), in which the coherent electrons oscillate as a longitudinal wave at extended metal surfaces[155].

LSPs from plasmonic nanomaterials can be excited by far-field incident light and can focus the light to a nanoscale edge, tip or crevice, thereby enhancing the local electromagnetic field intensity by two to five orders of magnitude. LSPs can also be excited by local oscillating sources (such as dipoles or quadrupoles) and directionally reradiate into the far field. Nanomaterials with tailored plasmonic characteristics have underpinned a vast array of applications in surface-enhanced spectroscopy, biosensors, subwavelength waveguides, nanolasers, metamaterials, plasmonic circuits and solar cells[156–160].

and microlithographic particle surfaces were widely explored[3,10,25] (FIG. 1). However, at that time, techniques to fabricate metallic structures at the nanometre scale were limited. PERS benefited considerably from developments in nanoscience in the 1990s[26]: in particular, from new techniques to synthesize and characterize SERS-active nanoparticles or nanostructures. Some examples of SERS-active nanostructures are Au and Ag nanoparticles with nanometre-sized gaps (nanogaps) and nanometre-sized tips (nanotips), and structured surfaces with nanometre-sized holes (nanoholes), voids, bumps, grooves or ridges[15,26–31] (FIG. 1). With the help of theoretical studies and the understanding gained from these nanostructured SERS substrates, researchers continue to develop new SERS substrates with much higher sensitivity[32–35] and for an expanding range of applications[36–40] (FIG. 1).

In the early stage, SERS was predominantly used to probe (sub-)monolayer molecules adsorbed on roughened coinage-metal surfaces or on metal colloids with an average SERS enhancement factor of 10^5–10^7 (FIG. 1). A great effort has been made to extend SERS for the surface analysis of various adlayer structures on other materials that are important to electrochemistry, corrosion inhibition and heterogeneous catalysis, such as Group VIIIB transition metals (Pt, Pd, Ru, Rh, Fe, Co and Ni)[38,39]. During the 1990s and 2000s, these transition metals, if prepared as appropriate nanomaterials, exhibited[38,41–44] weak SERS enhancement factors of the order of 10^1–10^3 (FIG. 1). Thus, the SERS enhancement factor of adsorbates on the surfaces of transition-metal nanomaterials is at least two to three orders of magnitude smaller than that of adsorbates on coinage-metal nanomaterials. As a consequence, it is still difficult to perform SERS analysis of general adsorbates, such as water molecules, on transition-metal surfaces.

To improve the SERS enhancement factor on transition-metal surfaces, a strategy (which we refer to as 'borrowing SERS') was devised to coat transition metals as an ultrathin shell or overlayer on the surface of Au and Ag nanostructures[26]. Boosted by the long-range effect of the enhanced electromagnetic field generated from the highly SERS-active Au or Ag cores, the chemisorption information of probe molecules on the transition-metal overcoating can be extracted by SERS measurements with an enhancement factor of up to 10^4–10^5. In principle, this strategy could be extended to probe other overcoating materials beyond metals without SERS activity on Au and Ag nanostructures (FIG. 1).

There are, however, several shortcomings of the borrowing SERS strategy. The SERS enhancement factor of the overcoating or shell material strongly depends on the thickness of the coating. In general, to obtain a strong SERS enhancement, the shell thickness should be less than 2 nm (that is, about seven atomic layers) for transition metals and 5 nm for dielectric materials. It is challenging to coat target materials, such as insulators or semiconductors, as an ultrathin shell on the surfaces of Au or Ag nanostructures. Furthermore, the shell should be free of pinholes in the coating materials to avoid the adsorption of analytes directly on the surface of Au or Ag nanostructures, which leads to misinterpretation of the Raman signal[15]. Moreover, in many

Box 2 | **Electromagnetic field enhancement in SERS**

Enhancement of the electromagnetic field in SERS is a two-step process[8,161]. First, local electromagnetic field enhancement occurs around the plasmonic nanoparticles (NPs) at the incident frequency (ω_0). In this step, plasmonic NPs serve as receiving optical antennae to transform the far field to the near field. Second, the enhancement arises from the Raman polarizability derivatives of the molecule–NP system, which are typically one to three orders of magnitude larger than those of the free molecules. This results from the strong mutual excitation between the induced dipole of molecules (short vertical arrows) and the dipole (and even multipoles) of the NPs (long vertical arrows). Here, the plasmonic NPs serve as transmitting optical antennae to transfer the near field to the far field at the Raman scattered frequency (ω_R). The enhancement factor in this step is proportional to the square of the local electric field ($\boldsymbol{E}_{loc}$) at ω_R.

For low-frequency vibrational modes of adsorbed molecules, the incident and Raman scattered frequency — and thus the enhancement factors of the first and second steps ($G_1(\omega_0)$ and $G_2(\omega_R)$, respectively) — are usually comparable. Therefore, the SERS enhancement factor is approximately proportional to the fourth power of the enhancement of the local electric field[162–165] (equation (1)), in which $\boldsymbol{E}_{loc}$ and $\boldsymbol{E}_0$ are the local electric fields in the presence and absence of nanoparticles, respectively.

$$G = G_1(\omega_0)G_2(\omega_R) = \frac{|\boldsymbol{E}_{loc}(\omega_0)|^2}{|\boldsymbol{E}_0(\omega_0)|^2}\frac{|\boldsymbol{E}_{loc}(\omega_R)|^2}{|\boldsymbol{E}_0(\omega_R)|^2} \approx \frac{|\boldsymbol{E}_{loc}(\omega_R)|^4}{|\boldsymbol{E}_0(\omega_0)|^4} \quad (1)$$

The local electromagnetic field in the gap between Au or Ag nanoparticle dimers and oligomers with interparticle nanogaps is extremely intense because of the strong electromagnetic coupling and can even support single-molecule detection[6,7,59,83,166–169]. Moreover, the electromagnetic field and SERS enhancement factors in the nanogap of Ag or Au oligomers strongly depend on the gap size. For example, when the gap size of a Au nanosphere dimer is reduced from 10 to 2 nm, the SERS enhancement factor increases[66,165,170] from 10^5 to 10^9. However, the local electromagnetic field and the SERS enhancement factor cannot be increased without a limit, because decreasing the gap size to the sub-nanometre scale introduces quantum effects between the coupled nanoparticles[171–173].

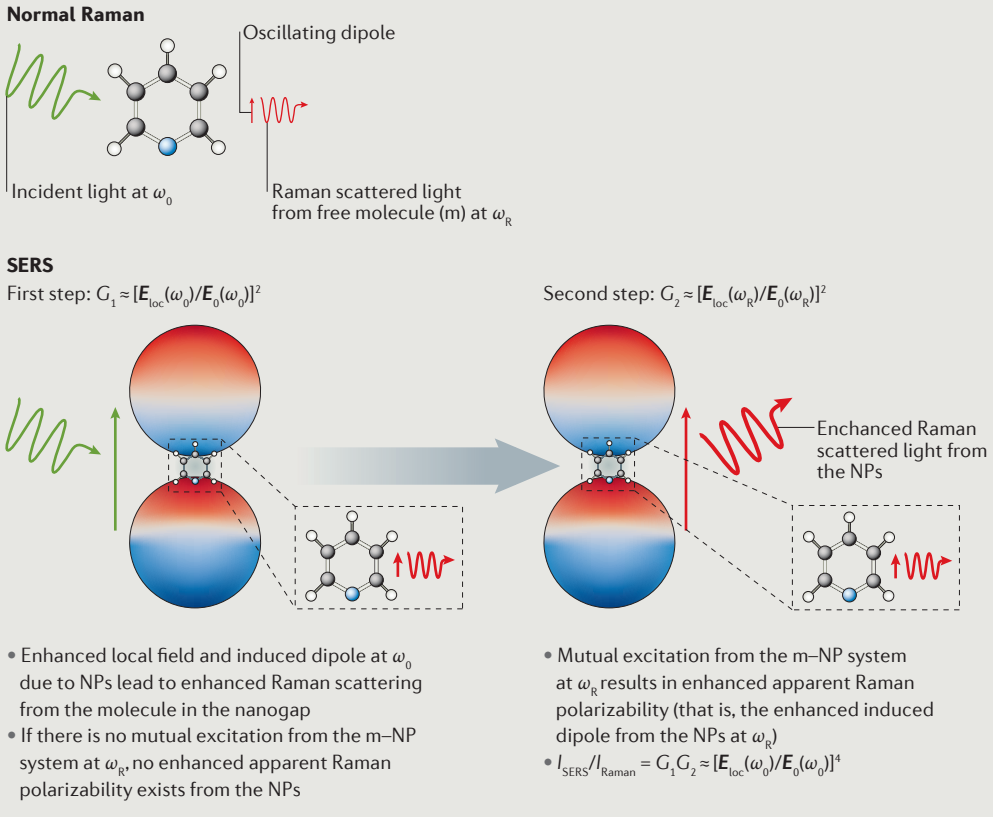

- Enhanced local field and induced dipole at ω_0 due to NPs lead to enhanced Raman scattering from the molecule in the nanogap
- If there is no mutual excitation from the m–NP system at ω_R, no enhanced apparent Raman polarizability exists from the NPs
- Mutual excitation from the m–NP system at ω_R results in enhanced apparent Raman polarizability (that is, the enhanced induced dipole from the NPs at ω_R)
- $I_{SERS}/I_{Raman} = G_1G_2 \approx [\boldsymbol{E}_{loc}(\omega_0)/\boldsymbol{E}_0(\omega_0)]^4$

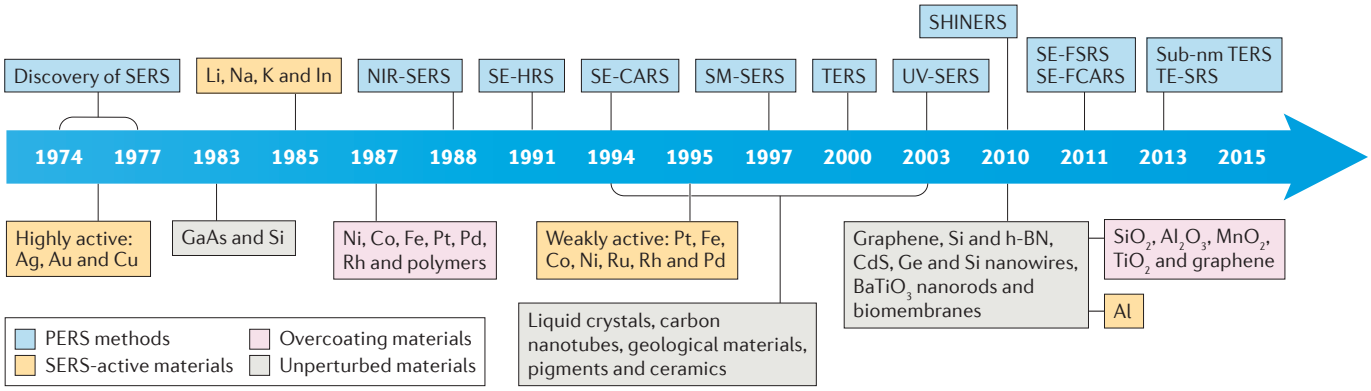

Figure 1 | **Key developments in PERS for material science.** NIR-SERS, near-infrared surface-enhanced Raman spectroscopy; PERS, plasmon-enhanced Raman spectroscopy; SE-CARS, surface-enhanced coherent anti-Stokes Raman spectroscopy; SE-FCARS, surface-enhanced femtosecond coherent anti-Stokes Raman spectroscopy; SE-FSRS, surface-enhanced femtosecond stimulated Raman spectroscopy; SE-HRS, surface-enhanced hyper-Raman spectroscopy; SHINERS; shell-isolated nanoparticle-enhanced Raman spectroscopy; SM-SERS, single-molecule surface-enhanced Raman spectroscopy; sub-nm TERS, tip-enhanced Raman spectroscopy with sub-nanometre resolution; TE-SRS, tip-enhanced stimulated Raman spectroscopy; UV-SERS, ultraviolet SERS.

cases, it is necessary to characterize the pristine surface structures of materials in their native environment for a given application. For example, the surface structures of silicon wafers and of blades in motors cannot be represented or modelled by an ultrathin structure or even a structure with nanoscale curvature. Therefore, new working modes of SERS were developed.

Two such working modes are those of TERS[11–14] and SHINERS[15], which yield giant Raman signals from unperturbed surfaces of general (that is, SERS-inactive) materials[45–47]. These new techniques provide a great opportunity to study the surfaces of a wide range of materials, including energy materials[48–51], electronic materials[15], optical materials, low-dimensional nanomaterials[52,53] and soft biomaterials[37,54] (FIG. 1).

More than 500 review articles on PERS have been published[24,45,55–60], and the total number of PERS-related publications is over 2,500 per year. However, most review articles are targeted to the physics, analytical chemistry and bioanalysis communities, with few written purely for the materials science community. In this Review, we address the fundamental issues associated with SERS for surface analysis and discuss the necessary working modes of PERS in the context of applications in fields such as catalysis, corrosion, energy materials, nanomaterials and molecular biology.

In the following section, we describe the first and second generations of SERS hotspots. We then discuss new, third-generation PERS hotspots generated by electromagnetic coupling in hybrid structures that contain both PERS-active nanostructures and probe materials. We focus our discussion on three key PERS working modes — contact-mode (SERS), shell-isolated mode (SHINERS) and non-contact mode (TERS) — and highlight recent advances in PERS applications in a range of material systems. Finally, we offer our perspective on the promising interplay between plasmon-enhanced spectroscopy and materials science, with an emphasis on new plasmonic materials and new nanostructures for PERS, and other plasmon-enhanced spectroscopic techniques.

First- and second-generation hotspots

The SERS enhancement factor is approximately proportional to the fourth power of the local electric field (BOX 2). More importantly, the electromagnetic field around plasmonic materials is not uniformly distributed but highly localized in spatially narrow regions (SERS hotspots), such as nanotips, interparticle nanogaps or particle–substrate nanogaps[45,61–71].

The first-generation hotspots were made from single nanostructures, such as nanospheres and nanocubes (FIG. 2a,b), or nanorods freely suspended in a homogeneous medium. These hotspots exhibit moderate SERS activity; however, some rationally designed single nanoparticles with sharp corners and/or with intraparticle gaps, such as Au and Ag nanostars, nanoflowers and mesocages, exhibit much higher SERS activity[72].

The second generation of SERS hotspots are generated from coupled nanostructures with controllable interparticle nanogaps (for example, the nanoparticle dimers shown in FIG. 2c,d, or oligomers and nanoparticle arrays shown in FIG. 2e,f) or interunit nanogaps in nanopatterned surfaces (FIG. 2g,h). Such hotspots exhibit excellent SERS activity. Because the average SERS intensities from coupled plasmonic nanostructures are typically two to four orders of magnitude greater than those from single nanostructures[66,73], they are more commonly used for trace-molecule detection.

The size of SERS hotspots from coupled nanostructures is extremely small (1–5 nm), but the Raman signals of probe molecules at the hotspots contribute significantly to the total Raman signal[74,75]. For example, the hotspot of a Ag nanosphere dimer (2-nm gap size) occupies less than 1% of the total area but can contribute more than 50% of the total SERS signal, provided that the molecules are uniformly distributed on the surface[64,76].

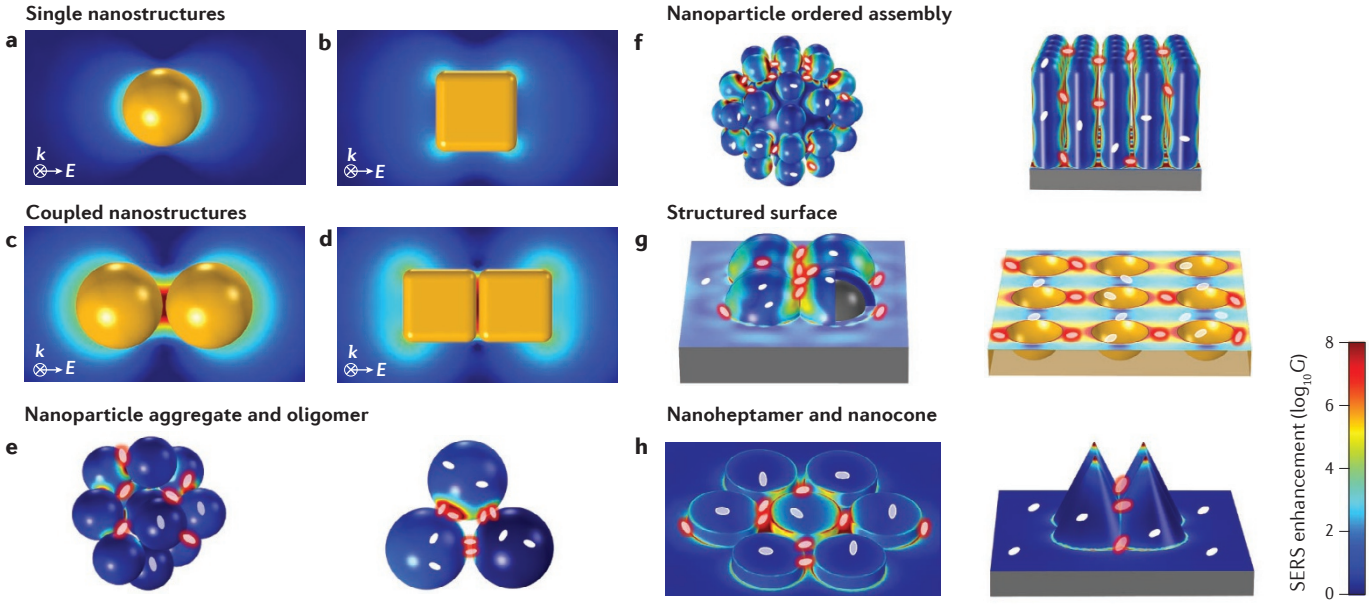

Figure 2 | **First- and second-generation SERS hotspots for trace-molecule detection. a–d** | Finite-element simulations of surface-enhanced Raman spectroscopy (SERS)-enhancement distribution in typical Au nanoparticles. Panel **a** shows a nanosphere with a diameter of 60 nm in water that has an excitation line at 545 nm ($<G_{NP}>=160$; $G_{NP}^{max}=2{,}500$). Panel **b** shows a nanocube with a side length of 60 nm that has an excitation line at 585 nm ($<G_{NP}>=1{,}400$; $G_{NP}^{max}=2{,}700$). Panel **c** shows a nanosphere dimer with a gap size of 2 nm in water that has an excitation line at 645 nm ($<G_{NP}>=1.47\times10^{6}$; $G_{NP}^{max}=4.11\times10^{9}$). Panel **d** shows a nanocube dimer with a gap size of 2 nm in water that has an excitation line at 725 nm ($<G_{NP}>=2.41\times10^{5}$; $G_{NP}^{max}=1.24\times10^{8}$). **e–h** | Schematic illustrations of typical coupled nanostructures as second-generation SERS hotspots for trace-molecule detection. Panel **e** shows Au nanoparticle aggregates with multiple hotspots (left) and an oligomer (right). Panel **f** shows a core–satellite nanostructured assembly with small Au nanoparticles assembled around a larger Au nanoparticle (left) or vertical self-assembly of Au nanorods on a support (right). Panel **g** shows nanostructured surfaces with nanobump (left) or nanovoid arrays (right) by deposition of Ag on the pre-assembled SiO_2 or polystyrene spheres. Panel **h** shows an individual nanoheptamer (left) and a nanocone quadrumer (right). In panels **e–h**, the adsorbed target molecules are depicted as white points. For the calculations, we used the experimental dielectric constants of Au from REF. 174, and of Si and Pt from REF. 175, and chose the resonance wavelength at the localized SPR peak, not the operation wavelengths of the lasers commonly used in SERS measurements. ***E***, electric field; $<G_{NP}>$, average SERS enhancement factor over the whole outer surface of a nanoparticle; G_{NP}^{max}, SERS maximum enhancement factor at the outer surface of a nanoparticle; ***k***, wavevector of incident light.

The extremely strong electromagnetic field in the tiny volume of the second-generation hotspots from coupled nanostructures is crucial for detecting and analysing trace amounts of molecules, including single molecules, located at the hotspots. An implication of this is that the probe molecule should be located at the hotspots.

Two main approaches (bottom-up and top-down) have been developed to prepare coupled nanostructures that can support second-generation hotspots for SERS. Bottom-up methods were first used to prepare highly monodispersed Au and Ag nanoparticle aggregates with dense SERS hotspots for application in the detection of trace molecules in the solution or gas phase[10,77]. However, nanoparticle aggregates are often not structurally well defined. Thus, high-yield and stable Au and Ag nanoparticle dimers and oligomers with well-defined nanogaps were prepared, to improve the reproducibility of single-molecule detection[30,33,78–83]. In addition, many more complex nanostructures were prepared using bottom-up approaches to improve the average SERS enhancement factor, such as core–satellite structures[84,85], nanoparticle assemblies with controllable nanogaps[27,74,86,87], and cauliflower-like[88] and other multi-branched nanostructures. Several new nanostructures have also been prepared by electrochemical or cold deposition of Au and Ag on prefabricated masks with dielectric nanoparticle assembly[29,89,90]. Highly ordered Ag nanoparticles with a controlled gap size (~2 nm) were also prepared by a nanocasting process using ordered mesoporous silica as the template[91].

Top-down techniques, such as electron-beam lithography, focused-ion beam and photon lithography, are also used to fabricate coupled nanostructures[75,92]. The advantage of top-down nanotechnology is its ability to fabricate SERS-active nanostructures with a wide range of geometries, ultrafine features, good reproducibility and large-scale uniformity[69]; examples include ordered clusters or arrays of pillars, holes, grooves and ridges with sharp corners and small gap size. Hierarchical structures, such as particle-in-cavity[93], particle-in-groove and particle-on-film[94,95] structures, have been developed for SERS analysis, because they can strengthen the plasmonic response and boost the overall SERS enhancement factor. However, challenges of top-down nanotechnology

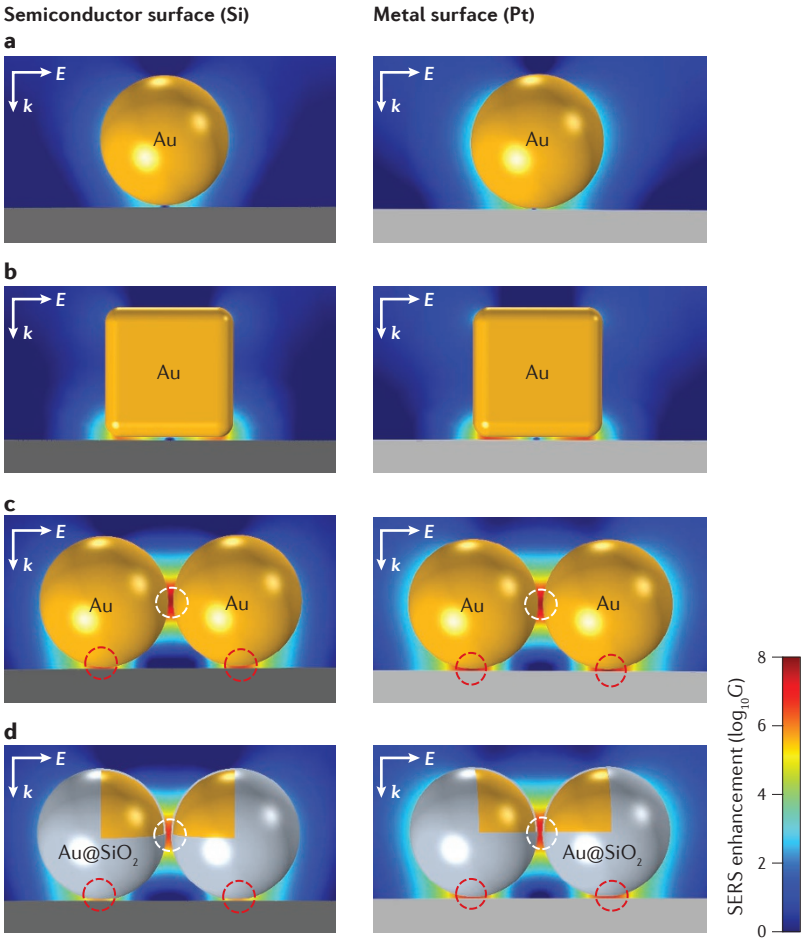

Figure 3 | **Third-generation hotspots for surface analysis. a–d** | Finite-element simulations of surface-enhanced Raman spectroscopy (SERS)-enhancement distribution for 'hybrid' nanostructures of SERS-active nanoparticles with Pt and Si probe materials. Panel **a** shows a bare Au nanosphere monomer on a Si surface (left) with an excitation at 530 nm ($<G_{sub}>=94$; $G_{sub}^{max}=2.03\times10^3$) and on a Pt surface (right) with an excitation at 535 nm ($<G_{sub}>=1.30\times10^3$; $G_{sub}^{max}=4.32\times10^4$). Panel **b** shows a bare Au nanocube monomer on a Si surface (left) with an excitation at 660 nm ($<G_{sub}>=1.48\times10^6$; $G_{sub}^{max}=1.42\times10^7$) and on a Pt surface (right) with an excitation at 825 nm ($<G_{sub}>=7.31\times10^5$; $G_{sub}^{max}=5.15\times10^6$). Panel **c** shows a bare Au nanosphere dimer on a Si surface (left) with an excitation at 600 nm ($<G_{sub}>=1.04\times10^5$; $G_{sub}^{max}=6.85\times10^6$; $G_{NP}^{max}=6.76\times10^7$) and on a Pt surface (right) with an excitation at 630 nm ($<G_{sub}>=1.02\times10^6$; $G_{sub}^{max}=9.01\times10^7$; $G_{NP}^{max}=7.19\times10^7$). Panel **d** shows a shell-isolated nanosphere ($Au@SiO_2$) dimer on a Si surface (left) with an excitation at 580 nm ($<G_{sub}>=1.74\times10^4$; $G_{sub}^{max}=8.37\times10^5$; $G_{NP}^{max}=6.56\times10^6$) and on a flat Pt surface (right) with an excitation at 600 nm ($<G_{sub}>=2.07\times10^5$; $G_{sub}^{max}=1.16\times10^7$; $G_{NP}^{max}=1.39\times10^7$). The diameter of the bare Au nanosphere and the core of the $Au@SiO_2$ is 60 nm, and the shell thickness of $Au@SiO_2$ is 2 nm. The size of the interparticle gap (in the region marked with a white dashed circle) in panels **c** and **d** is 2 nm and the particle–substrate gap (in the region marked with a red dashed circle) is 1 nm. ***E***, electric field; $<G_{NP}^{max}>$, SERS maximum enhancement factor at the outer surface of a nanoparticle; $<G_{sub}>$, average SERS enhancement factor at the substrate; G_{sub}^{max}, SERS maximum enhancement factor at the substrate; ***k***, wavevector of incident light.

lie in the difficulties in controlling the nanogap below 5 nm and the atomic-scale surface roughness.

At present, second-generation SERS hotspots are dominant in both fundamental and applied research. For example, hotspots are commonly designed for the verification of SERS mechanisms and the evaluation of the performance of newly developed nanostructures in SERS applications. Trace-molecule detection (for example, single-molecule detection in molecular electronics devices[96]) and biomolecule analysis (for example, pesticide residues, drugs, tumour and DNA sequences) have been successfully achieved[40,97–100]. In general, trace-molecule detection involves the probe molecules being attracted to and then 'squeezed' into the hotspots through diffusion, specific adsorption or target binding, and/or optical forces to optimize the SERS enhancement.

Third-generation hotspots

In general, first- and second-generation hotspots are not well suited for the surface analysis of many materials. For example, widely used materials, such as silicon wafer or ceramics, cannot be squeezed into the extremely tiny and narrow regions of the hotspots formed by coupled nanostructures, such as those shown in FIG. 2c–h. Therefore, it is highly desirable to design plasmonic nanostructures that can have hotspots right on the surface of the materials to be probed. This can be achieved by taking into account the effect of the materials to be probed when designing the plasmonic nanostructures, because the localized SPR response and local electromagnetic field distribution not only depend on the shape and size of these plasmonic nanostructures, but also depend sensitively on the dielectric properties of probe materials close to such nanostructures. Hotspots on probe material surfaces, which are generated from hybrid structures consisting of plasmonic nanostructures and the probe materials, can be considered third-generation hotspots. Representative examples are shown in FIG. 3.

The simplest example is a single Au nanoparticle on a flat Si or Pt surface[62,94,101–103] (FIG. 3a,b), in which a hotspot can be produced as a result of the hybridization of the electromagnetic field scattered from the nanoparticle and the electromagnetic field reflected from the material surface. The average SERS enhancement factor for a single Au nanosphere on a Pt surface (FIG. 3a, right) is about one order of magnitude larger than that of the nanosphere on a Si surface (FIG. 3a, left), owing to the plasmonic coupling between the Au nanoparticle and the Pt surface.

The enhancement can also be tuned by using different plasmonic nanostructures. For example, the average SERS enhancement factor over the projected area of a single Au nanocube on the Si surface (FIG. 3b, left) is about two orders of magnitude larger than that of a single Au nanosphere (FIG. 3a, left). When a bare Au nanosphere dimer is placed on a Si or Pt surface, hotspots can be simultaneously produced at the particle–substrate and interparticle nanogaps[70] (FIG. 3c) for a certain range of incident wavelengths. For dielectric materials (for example, Si), the average SERS enhancement factor at the surface in the presence of a Au nanosphere dimer (FIG. 3c, left) is about three orders of magnitude larger than that of a single Au nanosphere (FIG. 3a, left) at the surface. The average SERS enhancement factor increases with the refractive index of the dielectric material. For metal surfaces (for example, Pt), the average SERS enhancement factor at the surface in the presence of a Au nanosphere dimer (FIG. 3c, right) is about three orders of magnitude larger than that of a single Au nanosphere

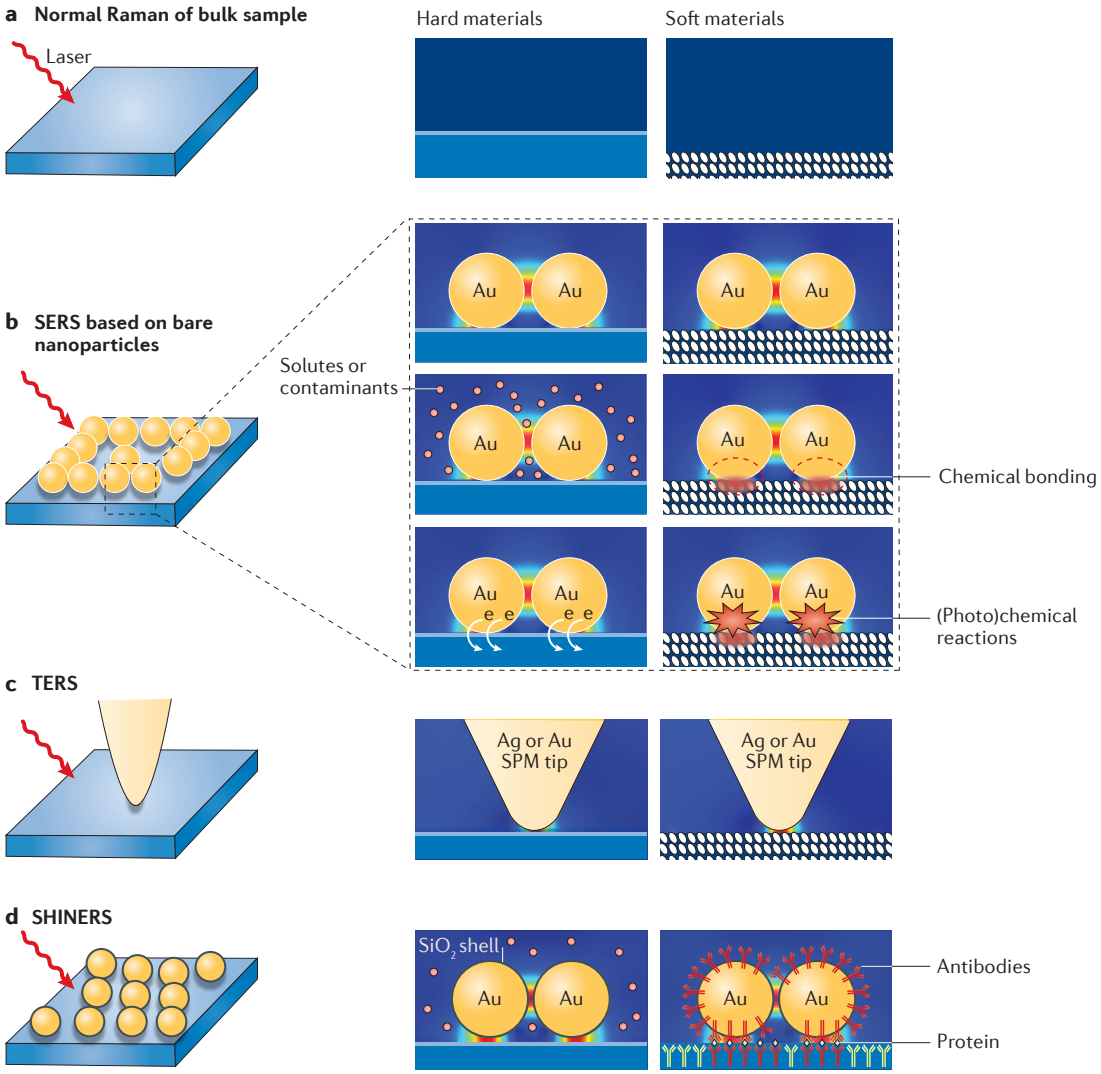

Figure 4 | **Different measurement modes of Raman and PERS on hard and soft materials. a** | Raman measurements on bulk samples comprise signals mainly from the bulk. **b** | Surface-enhanced Raman spectroscopy (SERS) measurements on probe materials in vacuum or in ambient conditions, on solid/liquid or solid/air interfaces in which solute molecules in solution or contaminants in air can be directly adsorbed on bare Au nanoparticles, on soft surfaces with chemical bonding or (photo)chemical reactions in the presence of bare Au nanoparticles, and on hard surfaces with interfacial charge transfer between bare Au nanoparticles and the hard probe material. **c** | Tip-enhanced Raman spectroscopy (TERS) measurements of hard and soft materials. **d** | Shell-isolated nanoparticle-enhanced Raman spectroscopy (SHINERS) measurements of solid/liquid interfaces, which can avoid contaminants being specifically adsorbed on the surfaces of bare Au nanoparticles (left), and shell-isolated nanoparticles functionalized with antibodies for sensitive detection of protein targets (right). In the calculations, we used the wavelength with the largest plasmon-enhanced Raman spectroscopy (PERS) average enhancement rather than the wavelengths of the lasers commonly used in SERS measurements. SPM, scanning probe microscope.

(FIG. 3a, right) at the surface, owing to the additional plasmonic coupling between the Au nanosphere dimer and the metal surface[70]. When a shell-isolated Au@SiO_2 dimer is placed on a Si or Pt surface, hotspots can be simultaneously produced at the particle–substrate and antiparticle nanogaps (FIG. 3d). Additionally, the chemically inert shell can avoid unwanted or unexpected interfering signals from the interfaces. To obtain higher sensitivity, nanoparticle clusters can be used instead of single nanoparticles on the surface of the probe material. The SERS enhancement also significantly depends on the particle–substrate nanogap, and on the wavelength and polarization states of the incident laser.

Contact-mode SERS for surface characterization. Third-generation hotspots can be realized in three different working modes (FIG. 4). The earliest and simplest is contact-mode SERS (FIG. 4b), in which SERS-active bare Au or Ag nanoparticles are coated on the surface of the probe material to enhance the surface Raman

signals[104]. The bare nanoparticles either directly contact the probe material surface or contact self-assembled probe molecule layers on a metal substrate (the latter is referred to as gap-mode SERS in the literature[62,67,94,105]).

Contact-mode SERS exhibits excellent enhanced Raman signals in various applications; however, it has several significant limitations, which may be why it has not been more widely adopted by the materials science community in the past three decades. For example, solute molecules or contaminants in solution or gas can easily be adsorbed on the surfaces of the bare Au nanoparticles most commonly used in SERS and can then diffuse into the particle–substrate hotspots (FIG. 4b). As a consequence, the SERS spectra might be dominated by contaminated Raman signals, leading to the misinterpretation of SERS spectra of adsorption and surface processes.

In addition, interfacial charge transfer may occur between some hard materials (such as Pt, Ni or Co) and bare Au or Ag nanoparticles because of their differences in work functions (FIG. 4b). Unwanted interference may be stronger for soft materials (such as liquid crystals, polymer films and molecular self-assemblies), because the contact of bare Au nanoparticles may result in the formation of new chemical bonds or induce a photochemical reaction under strong laser illumination[15] (FIG. 4b). Therefore, one must be cautious about interference from the direct contact between bare Au or Ag nanoparticles and the probe material to avoid misinterpretation of the surface Raman spectra[47]. Moreover, for hybrid structures including single or clustered Au or Ag nanoparticles on a metal substrate, the nanoparticles and the metal substrate may fuse under strong laser illumination. The fusion of Au or Ag nanoparticles with the metal substrates damages the hybrid structure, thereby adversely affecting the local electromagnetic field distribution and the SERS performance of hybrid structures. Accordingly, probe adsorbates on fused metal surfaces also affect the original surface Raman spectra of probe molecules on the metal substrates.

To overcome these drawbacks of contact-mode SERS, two working modes with more versatile and reliable surface analysis capability have been developed: TERS, which operates in non-contact mode, and SHINERS (FIG. 4c,d). These two modes can support third-generation hotspots and the details are discussed in the following two sections.

TERS. TERS was invented[11–14] in 2000, with the aim of realizing ultrahigh spatial resolution. After 15 years of development, TERS has found important applications in the nanoscale chemical analysis of functional materials (for example, ferroelectric or photo-conversion materials), carbon nanotubes, graphene, semiconductor materials, polymers, biomolecules and even single molecules[46,106,107].

Although other methods can characterize the surface morphology of materials with atomic resolution, it remains challenging to investigate the structure, chemical composition and morphology of material surfaces simultaneously. TERS combines the advantages of scanning probe microscopy (that is, high spatial resolution) and SERS (that is, highly sensitive molecular information). In TERS, a plasmonic Au or Ag tip with a radius of about 20 nm is used to create a single hotspot between the tip and the probe material. When the tip approaches a sample surface, the electromagnetic field and the Raman signal of the sample are significantly enhanced to provide high detection sensitivity[46] (FIG. 4c). Because the enhanced field is highly localized to the tip apex, it can selectively probe the local chemical and electronic structure at a spatial resolution of about 10 nm.

In contrast to SERS and SHINERS (described in the following section), TERS offers only one hotspot for Raman measurements. Thus, its sensitivity is typically much lower than that of SERS and SHINERS. However, TERS provides nanometre spatial resolution, which is not achievable with either SHINERS or SERS. If a metallic or dielectric material with a high refractive index is to be investigated, gap-mode TERS can be used to improve the field enhancement, sensitivity and spatial resolution[14].

SHINERS. SHINERS was invented[15] in 2010 and uses shell-isolated nanoparticles composed of plasmonic Au or Ag cores with ultrathin (1–5 nm) and chemically and electrically inert shells (for example, of SiO_2 or Al_2O_3). The advantages of SHINERS are fourfold. First, the ultrathin yet pinhole-free shells separate the cores from the material surface (and the environment), thus ensuring that there is almost no interference from Au and Ag cores. Second, the chemically inert shell effectively avoids interparticle and particle–metal substrate fusion, which significantly improves the stability of the nanoparticles and the probe structures. Third, the shell thickness can be used to control the nanogap between the Au or Ag core particle and the substrate, and consequently determines the particle–substrate electromagnetic coupling. Last, the Au and Ag cores can boost the local electromagnetic field to enhance the Raman signals from the probe substrate without distorting its structure[15,108] (FIG. 3d).

The shell-isolated mode in SHINERS is different from contact-mode SERS in that the probe materials cannot directly interact with the Au and Ag cores because of the inert, isolating ultrathin shells (FIG. 4d). Because it is implicit in the name SERS that the surface of the SPR-active nanostructure directly touches the probe target (either molecules or materials), SHINERS cannot be classified as a SERS technique[15]. This is also true for TERS. Because SERS, TERS and SHINERS involve local field enhancement due mainly to the enhancement of SPR, each can be considered as a unique PERS technique.

SHINERS overcomes several disadvantages of contact-mode SERS for surface analysis but at the cost of reduced Raman enhancement. Both interparticle plasmonic coupling and nanoparticle–substrate coupling in shell-isolated nanoparticle-on-substrate systems are moderate when compared with bare nanoparticle-on-substrate systems. The average SHINERS enhancement factor is about six and five times weaker than that from a bare Au nanoparticle dimer on Si and Pt surfaces, respectively (FIG. 3c,d).

In practice, shell-isolated nanoparticles are simply spread as 'smart dust' over the surfaces of materials with diverse compositions and morphologies[15].

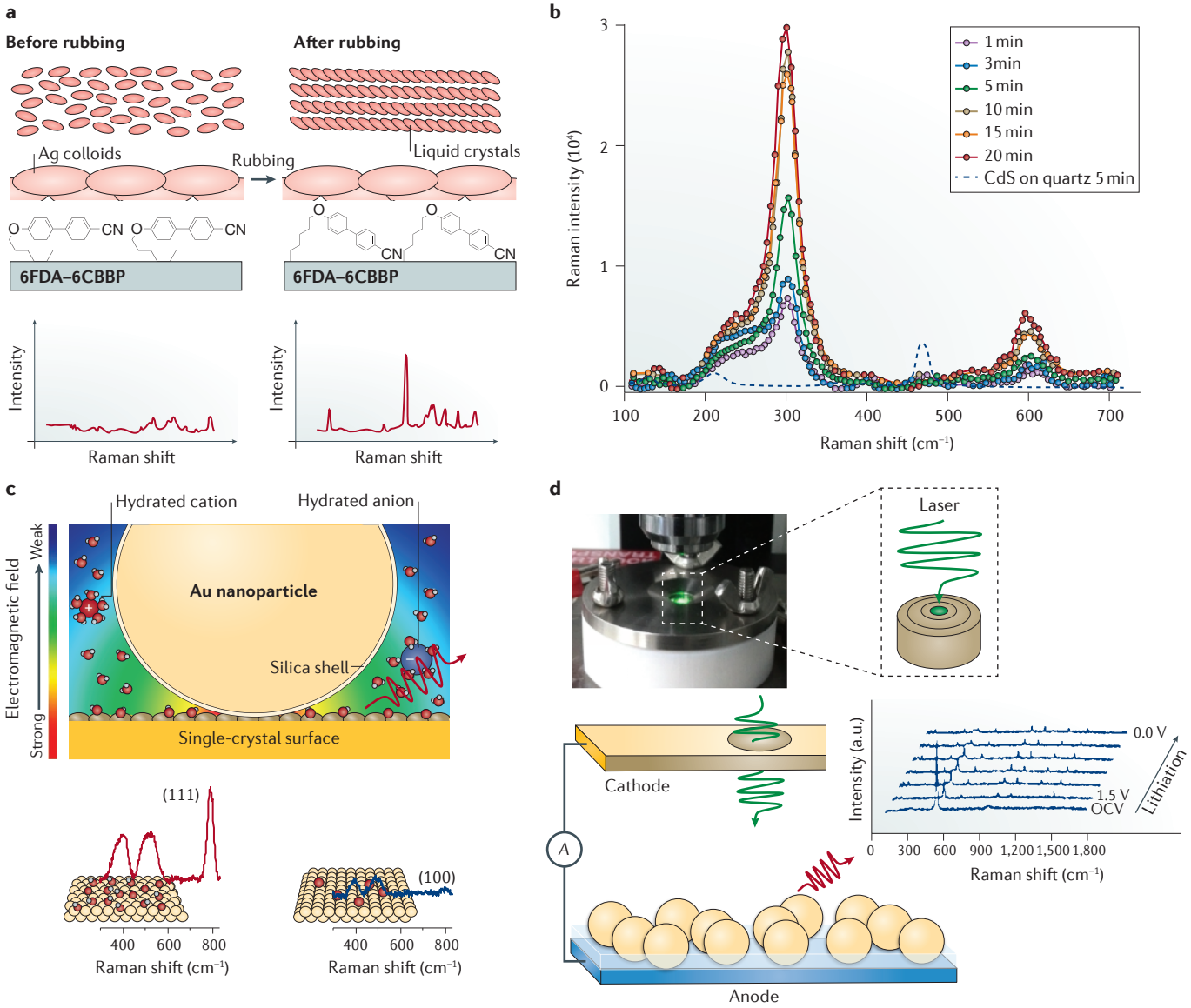

Figure 5 | **Selected applications of SERS and SHINERS in material systems. a** | Surface-enhanced Raman spectroscopy (SERS) measurements in a liquid-crystal system. Ag colloids were deposited on a polyimide layer (6FDA–6CBBP) that can control the bulk orientation of liquid crystals. Distinct Raman spectra were obtained before and after rubbing the polyimide layers. **b** | SERS study of CdS growth kinetics during the early stages of liquid-phase chemical bath deposition. The Raman intensity of CdS saturates after 10 minutes of deposition, which is indicative of 3D deposition. **c** | Schematic illustration of shell-isolated nanoparticles at an atomically flat single-crystal surface and *in situ* monitoring of surface electrooxidation of Au(*hkl*) surfaces. **d** | *In situ* shell-isolated nanoparticle-enhanced Raman spectroscopy (SHINERS) study of solid electrolyte interphase formation on the surface of a Si electrode in a Li-ion battery. The shell-isolated nanoparticles ($Au@SiO_2$) were deposited on the electrode surface before the assembly of the coin cell. A small hole was made through the top cap, Li foil and separator for the laser to enter and the Raman signal to exit the cell. a.u., arbitrary units; OCV, open-circuit voltage. Panel **b** is adapted with permission from REF. 110, American Chemical Society.

However, SHINERS requires high-quality, pinhole-free shell-isolated nanoparticles. Therefore, if the aforementioned limitations due to bare nanoparticles are acceptable for a given application, it is appropriate to use SERS with bare nanoparticles to attain a higher sensitivity than SHINERS. However, when interference effects due to bare nanoparticles are severe, SHINERS is the technique of choice.

Applications of SERS, TERS and SHINERS

Applications based on third-generation hotspots using SERS, TERS and SHINERS can be divided into two categories. The first is the surface characterization of materials such as liquid crystals, silicon or polymers, in which the structure of the surface may be different from the bulk one, as well as nanomaterials, such as graphene, carbon nanotubes and magnetic

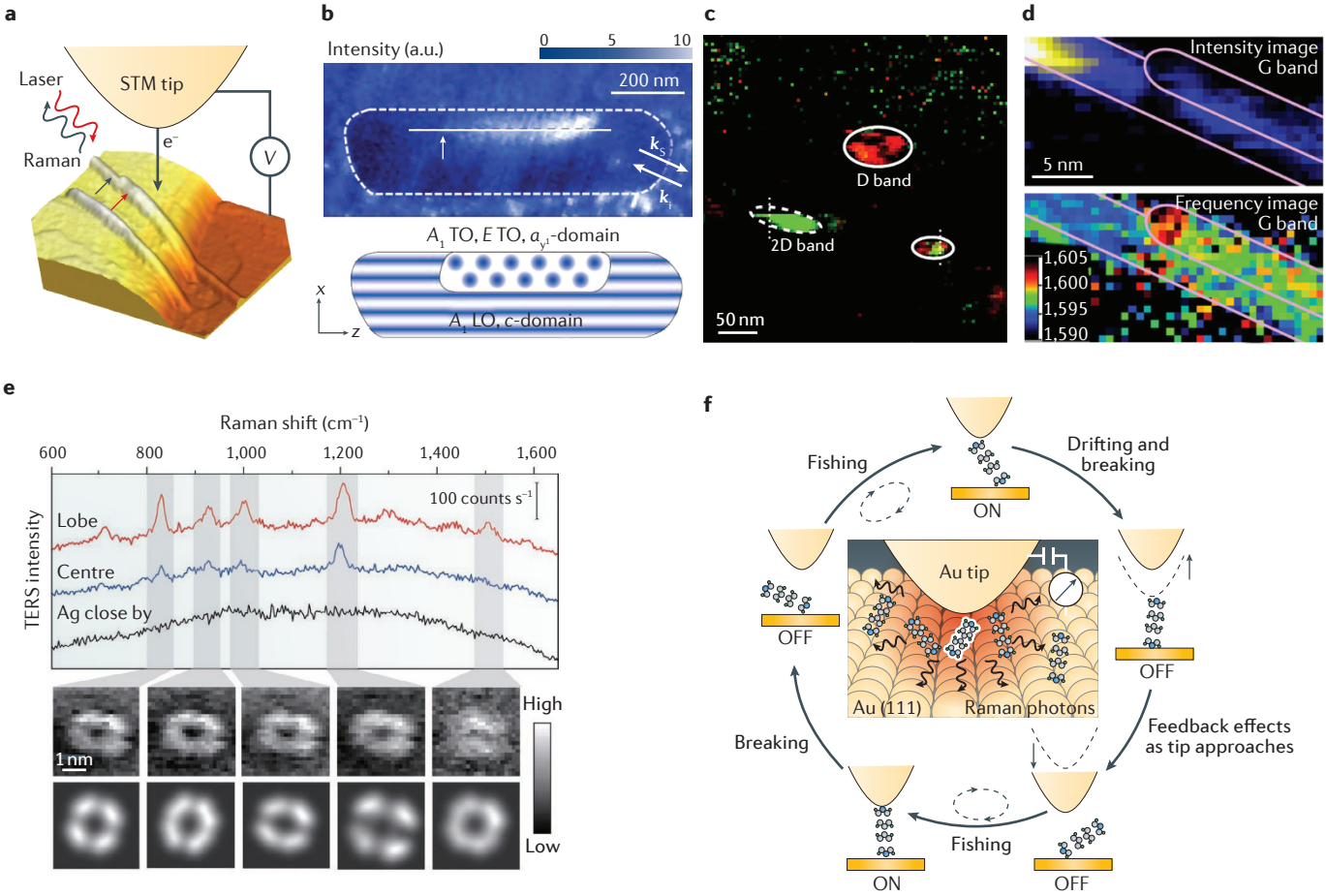

Figure 6 | **Selected examples of TERS applications in material systems. a** | Schematic illustration of the principle of scanning tunnelling microscopy (STM)-based tip-enhanced Raman spectroscopy (TERS). **b** | TERS image of a $BaTiO_3$ nanorod showing the ferroelectric domain with the domain assignment depicted below. A_1 TO and E TO are assigned to the transverse optical mode with A_1 and E symmetry in the a_y-domain, respectively; A_1 LO is assigned to the longitudinal optical mode with A_1 symmetry in the c-domain; $\mathbf{k}_s$ and $\mathbf{k}_i$ are the wavevectors of scattering and incident light, respectively. **c** | Overlapped TERS image of graphene on Au substrate using the D band signature of the defects and the 2D band signature of the single-layer graphene; the spatial resolution is better than 12 nm. **d** | TERS image of a single-wall carbon nanotube bundle obtained using the intensity and frequency shift of the G band; the spatial resolution is 1.7 nm. The purple line in the image is to indicate the outline of the two tubes. **e** | Experimental and simulated TERS images of a single porphyrin molecule on a Ag(111) surface and of the nearby Ag surface. **f** | Fishing-mode TERS applied to simultaneously obtain single-molecule conductance and the TERS spectra for the Au–4,4-bipyridine–Au molecular junction. a.u. arbitary units. Panel **a** is from REF. 53, Nature Publishing Group. Panel **b** is from REF. 112, Nature Publishing Group. Panel **c** is adapted with permission from REF. 52, American Chemical Society. Panel **d** is from REF. 53, Nature Publishing Group. Panel **e** is from REF. 114, Nature Publishing Group. Panel **f** is from REF. 118, Nature Publishing Group.

nanocrystals. The second category is the determination of the molecular composition and surface bonding of molecular adlayers or surface species interacting with the substrate, such as oxygen species on Pt, hydrogen on Si, corrosion inhibitors on stainless steel or self-assembled layers on structured materials. PERS can be used to investigate several interface-related processes such as growth kinetics of films, mechanically induced conformational changes, ion-intercalation processes, corrosion and electrocatalysis. Some selective examples are shown in FIG. 5 and detailed in the following sections. Such investigations would greatly deepen our fundamental understanding of the structure–property relationships of emerging materials.

Applications of contact-mode SERS. Polyimide alignment layers (PALs) with high pretilt angles have a crucial role in controlling the orientation of liquid crystals. By mechanical rubbing of the PALs, as shown in FIG. 5a, the bulk orientation of liquid crystals can be controlled in a preferential direction by interface-induced alignment between the liquid crystals and PALs. However, this phenomenon, as well as the surface structures of the PALs before and after rubbing, is not well understood. SERS with bare Ag colloids has been used to reveal that both the pendent cyanobiphenyls in the side chains and backbones in the first PALs possess nearly planar chain conformations before surface rubbing[109]. After rubbing, some of the backbone moieties (for example,

imide-phenylene) tilted, and the conformation of the pendent side chains at the surface was significantly different (FIG. 5a). This conformational rearrangement of the side chains resulted in the formation of fold-like bent structures on the surface, which directly leads to a large negative pretilt angle of the long axis of cyanobiphenyls with respect to the rubbing direction.

Liquid-phase chemical bath deposition is an important technique for depositing metals, semiconductors and dielectric thin films over large areas because of its low cost and scalability. However, *in situ* characterization of the growth kinetics during the early stages is challenging. SERS was recently used[110] to study the early-stage growth kinetics during the liquid-phase chemical bath deposition of CdS. No Raman signal was observed for the CdS film after 5 minutes of deposition on a pure quartz surface; by contrast, the Raman signal (with peaks at 305 and 600 cm^{-1}) of CdS on Ag nanoparticles was pronounced and increased with deposition time. Interestingly, the Raman intensity of CdS saturated after 10 minutes of deposition (~20-nm thickness), which can be explained in terms of preferential deposition of CdS on itself (FIG. 5b).

Vanadium oxide is an abundant, low-cost metal oxide that is well suited for ion intercalation. In a recent study[111], SERS was used to probe the ion-intercalating processes in electrodes by placing a bare single Au nanoparticle on a vanadium oxide surface to form a Au nanoparticle–dithiol–vanadium oxide nanojunction. When cycling the electrochemical potentials, real-time chemical and structural changes (obtained through variations of the Raman frequencies and intensities) were found to correlate with ion intercalation–extraction processes at the vanadium oxide/electrolyte interface. Thus, this study provided a unique SERS-based strategy to probe ion intercalation processes.

Applications of TERS. A typical STM-based TERS set-up is illustrated in FIG. 6a. The tip is brought to about 1 nm from the material surface, which is then illuminated by a laser of suitable wavelength. As the tip is scanned over the surface, a TERS image of the Raman characteristics of the material can be obtained with high spatial resolution.

Barium titanate, $BaTiO_3$, is an important ferroelectric perovskite material used in piezoelectric actuators and non-volatile memory. The nanoscale characterization of this material may lead to a fundamental understanding of its nanoscale ferroelectric order and domain behaviour. TERS is a particularly powerful technique for characterizing the phases in crystal domains. For example, the Raman-active longitudinal optical mode of $BaTiO_3$ is characteristic of the tetragonal phase and is a marker of the ferroelectric state[112]. Ferroelectric domains have been successfully identified in a $BaTiO_3$ nanorod using TERS at a spatial resolution that is not obtainable using a conventional Raman microscope (FIG. 6b). The lattice constants differ by only 0.044 Å between the cubic paraelectric phase and the tetragonal ferroelectric phase, making their distinction difficult to observe even with high-resolution transmission electron microscopy in combination with electron diffraction techniques. However, TERS can be used to sensitively identify the difference between phases, and it has great potential in characterizing ferroelectric materials.

Chemical analysis of defects, strain and surface chemistry at nanometre resolution is highly desirable in carbon materials, including carbon nanotubes and graphene. Recently, TERS has been used for chemical analysis of single-layer graphene on a Au substrate[52]. Using the 2D-band (2,662 cm^{-1}) signature of single-layer graphene and the D-band (1,350 cm^{-1}) signature of the defects, a spatial resolution of better than 12 nm was obtained, with full spectral information in every pixel. Two defects within the surrounding graphene layer were clearly identified (FIG. 6c). In a separate study[53], 1.7-nm spatial resolution was achieved under ambient conditions, simultaneously providing chemical and topological information of individual carbon nanotubes. In this study, different types of carbon nanotubes, local defects and bundling effects were visualized in real space, as shown in FIG. 6d. Most importantly, this method does not rely on an ultrahigh-vacuum and cryogenic environment and is suitable for analysing soft materials, which is not possible with general electron microscopy techniques. More recently, TERS has been successfully used to plasmonically generate and detect spin waves (a collective oscillation of spin moments in a crystal, which may have an important role in spintronics) in α-Fe_2O_3 nanocrystals[113]. The two-magnon mode (spin wave) of α-Fe_2O_3 nanoparticles, which is not observable in bulk materials, becomes prominent at 1,587 cm^{-1} in the TERS spectrum as a result of phonon-mediated coupling of the spin of *d*-orbital electrons with the strongly localized electromagnetic field in the vicinity of the tip apex.

In gap-mode TERS, if the localized SPR of a Ag tip and Ag substrate is tuned to match the electronic resonance of the molecule, the local field may be further confined to produce ultrahigh spatial resolution. Such tuning can be realized by vacuum bombardment of the Ag tip. An ultrastable, low-temperature and ultrahigh-vacuum STM in the TERS system can efficiently prevent thermal drift of the STM system and suppress lateral movement of the molecule. This approach allows spatial resolution of TERS on the sub-nanometre scale and has been applied to resolve the structure and configuration of a single porphyrin molecule on a surface[114], as shown in FIG. 6e. Different vibrational modes show slightly different patterns. Although the detailed mechanism underlying this unprecedented spatial resolution is still under debate, this work has already launched a surge of theoretical work[115–117].

TERS can be used not only to characterize materials under static conditions as described above, but also to probe dynamic processes. In molecular electronics, the molecular structure and interface between the molecule and conducting lead are two of the most important criteria in searching for suitable materials. It remains a great challenge to characterize and gain detailed structural information of the molecule–metal–molecule junction during the electron transport. Fishing-mode TERS was developed to increase the probability of forming a

Au–4,4′-bipyridine–Au junction in the gap between a Au tip and Au substrate[118] (FIG. 6f). This allows mutually verifiable single-molecule conductance and Raman signals with single-molecule contributions to be acquired simultaneously under ambient conditions, which is not achievable using conventional techniques (for example, ultrahigh-vacuum-based inelastic electron tunnelling spectroscopy). The conducting molecular junctions had a Raman signature that was distinct from the broken molecular junctions. Such a strong bonding interaction between the molecule and the drain may account for the nonlinear dependence of the conductance on the bias voltage.

Owing to its high spatial resolution under ambient conditions, TERS can also be applied to reveal conformational changes in biomaterials: for example, the secondary structure (that is, of the α-helix and β-sheet) on fibril surfaces with a lateral resolution better than 2 nm (REF. 119). The commercialization of TERS instruments and the fast development of nanoscale infrared spectroscopy make it very likely that nanoscale vibrational spectroscopy will have an important role in future nanoscale chemical analysis.

To analyse complex chemical reactions at surfaces, it is necessary to use PERS methods under *in situ* conditions, whereby, for example, they operate under an applied voltage in the case of electrochemical systems and under light illumination in the case of photocatalytic systems. Electrochemical TERS is a particularly promising recent development in this area, because it can easily tune the electronic state of the electrode surface, with the laser focused in the gap between the tip and electrode surface. This offers a flexible way to control and characterize the surface reaction at the nanometre scale[120].

Applications of SHINERS. Single-crystal surfaces with atomically flat and well-defined surface states are the model systems for many fundamental studies (for example, heterogeneous catalysis). To circumvent the previously discussed issue of interference in contact-mode SERS, SHINERS has been successfully used to study the relationship between surface structures of materials and their reactivity. By simply casting Au nanoparticles coated with SiO_2 (Au@SiO_2) at Au(*hkl*) electrodes, surface Raman signals have been obtained during the electrooxidation of a single-crystal Au surface[51] (FIG. 5c). The Au–OH bending mode (δ_{AuOH}) at ~790 cm^{-1} was detected at the beginning of the Au oxidation process and diminished after complete oxidation of the Au surface. This finding provided the first direct insight into the chemical nature of the intermediate species, which had long been under speculation. Moreover, the intensities of the bending mode δ_{AuOH} at three single-crystal facets increased in the order of Au(100) < Au(110) << Au(111), which revealed that the surface coverage of hydroxide species is very sensitive to the crystal orientation of the surface. Interestingly, this order is the opposite to the order of activity in the oxygen reduction reaction under the same conditions. This may be because hydroxide ions formed during Au reduction retard the oxygen reduction reaction. *In situ* electrochemical SHINERS offers a unique opportunity for a real-time investigation of electro- and photocatalytic reactions, as well as corrosion inhibitors[121] at structurally well-defined surfaces.

The formation of interfacial species in Li-ion batteries strongly influences the battery performance. SHINERS has also been used to monitor interfacial processes in Li-ion batteries *in situ*[49]. In this study, the SHINERS

Table 1 | **Future directions of plasmon-enhanced spectroscopy in materials science.**

Category	UV	Visible	NIR	MIR	FIR
Wavelength	100–380 nm	380–760 nm	0.76–3 μm	3–50 μm	50–1,000 μm
Energy	12.4–3.1 eV	3.26–1.63 eV	1.63–0.41 eV	410–24.8 meV	24.8–1.24 meV
Alternative plasmonic materials	Al, Ga, In, Sn, Tl, Pb, Bi, Pd and Rh	Au, Ag, Cu and their alloys; metal nitrides (TiN and ZrN), silicides, borides and germanides	TCO: ITO, Al:ZnO, Ga:ZnO, n-GaAs, n-InP and n-Si	SiC, InAs, InSb, Si:GaAs, NiSi, TiSi, GaN, hybrids with noble metals and graphene	Graphene and Sn:In_2O_3
New structures	Similar structures to those in the visible region but with UV plasmonic materials.	• Nanostructures supporting hotspots on surfaces: nanocubes, nanobars and concave nanocrystals • Ultrathin dielectric-shell nanoparticles: Ag@SiO_2, Ag@MnO_2 and Ag@ZrO_2	Hierarchical structures with a metal NIR optical antenna and with a plasmonic nanogap and/or nanotip	Hierarchical structures with a metal MIR optical antenna (periodic metal grooves, holes or microholes) with plasmonic MIR nanostructures (such as graphene nanoribbons)	• Graphene nanoribbons, nanoporous graphene • Hierarchical structures with a metal FIR optical antenna with plasmonic FIR nanostructures (such as nanotips and nanocubes)
New spectroscopic techniques	UV-SERS, SE-RRS, possibly SE-RROA and possibly UV-SE-FSRS	SEF, SE-SFG and SE-ROA	NIR-SERS, SE-NIRAS and possibly NIR-SE-FSRS	SE-IRAS, SE-IRSS and possibly TE-IRS	Possibly TE-THz

FIR, MIR, NIR, far-, mid- and near-infrared, respectively; ITO, indium tin oxide; NIR-SERS, near-infrared surface-enhanced Raman spectroscopy; SEF, surface-enhanced fluorescence; SE-IRAS, surface-enhanced infrared absorption spectroscopy; SE-IRSS, surface-enhanced infrared scattering spectroscopy; SE-NIRAS, surface-enhanced near-infrared absorption spectroscopy; SE-ROA, surface-enhanced Raman optical activity; SE-RROA, surface-enhanced resonance Raman optical activity; SE-RRS, surface-enhanced resonance Raman spectroscopy; SE-SFG, surface-enhanced sum-frequency generation; TCO, transparent conducting oxide; TE-IRS, tip-enhanced infrared spectroscopy; TE-THz, tip-enhanced terahertz spectroscopy; UV-SE-FSRS, ultraviolet surface-enhanced femtosecond stimulated Raman spectroscopy; UV-SERS, ultraviolet surface-enhanced Raman spectroscopy.

signals were identified to relate to the formation of a solid electrolyte interphase on the Si electrode before reduction of ethylene carbonate during charge–discharge cycling (FIG. 5d). In contrast to the normal Raman signal from the bulk Si electrode, the SHINERS signal revealed different amorphization rates at the surface and bulk of the electrode. SHINERS has further been applied to directly observe the formation of Li_2O during electrochemical cycling on a Li-rich cathode. Formation of Li_2O on the cathode leads to the generation of H_2O and LiOH, as well as changes in the electrolyte, which eventually results in a deterioration in performance[50]. Thus, SHINERS offers a unique method to deepen our understanding of surface reactions that heavily influence the overall battery performance.

Silicon is currently the most important semiconductor material in the electronic industry. SHINERS can be used to analyse the surface functional groups by simply drop coating shell-isolated nanoparticles at atomically flat Si surfaces[15,122]. A strong Si–H band at about 2,149 cm^{-1} was observed[15] when the surface was treated with HF solution, which disappeared after O_2 plasma treatment. This example demonstrates the great potential that SHINERS holds in unravelling interfacial phenomena that occur during industrial processing of semiconductors, as well as in various chemical or electrochemical processes. This technique has also been used to characterize the structures of living bacteria (for example, the yeast cell wall) and to detect pesticide residues on fruits and vegetables for food safety.

Perspectives

To further expand the applications of PERS in materials science, it is necessary to improve the enhancement and spatial resolution. Progress in materials science — especially in nanomaterials — has aided the development of PERS, which, in turn, has greatly contributed to our understanding in many branches of materials science. However, this mutually beneficial relationship is still in its infancy. Below, we detail some of the directions that this field will take in the near future, the materials that will enable this and the materials systems that will benefit from these advances.

New plasmonic materials for a broader wavelength range. The success of PERS relies on the development of new nanostructures in the visible and near-infrared region. Several alternative plasmonic materials beyond coinage metals have been predicted or even developed, including metal nitrides, silicides, borides and germanides for visible plasmonics[123–127] (TABLE 1).

Other new plasmonic materials have been explored that might enable PERS to be carried out in different wavelength regions. Some examples (also listed in TABLE 1) include Al, Ga, In, Sn, Tl, Pb and Bi for ultraviolet plasmonics[128]; transparent conductive oxides, including indium tin oxide, Al:ZnO and Ga:ZnO; n-type semiconductors, including n-GaAs, n-InP and n-Si for near-infrared plasmonics; III–V or IV–IV semiconductors for mid-infrared plasmonics[129]; and $Sn:In_2O_3$ and graphene for terahertz plasmonics[130,131]. These alternative plasmonic materials will pave the way for diverse applications, including plasmon-enhanced spectroscopy, localized SPR sensing, superlenses and negative-index metamaterials[123].

New nanostructures for third-generation PERS hotspots. Electromagnetic coupling in hybrid structures should be carefully considered when designing PERS-active nanomaterials for materials analysis. In practice, the electromagnetic coupling in hybrid structures of Au or Ag nanoparticle clusters on metallic substrates can be very strong if the particle–substrate nanogap can be well controlled, as is the case with the shell-isolated strategy. But for hybrid structures with Au or Ag nanoparticle clusters on dielectric material substrates with a low refractive index, such as SiO_2 and biomembranes, only a small proportion of hotspots is located at the material surface.

One possible way to overcome this problem is to develop Au and Ag nanocrystals with sharp corners (for example, nanocubes, nanobars or concave nanocrystals) that support stronger intraparticle electromagnetic coupling[101,132,133]. It is also possible to create spoof surface plasmons using prism-coupling attenuated-total-reflectance based on periodic metal grooves that are fabricated on thin Au or Ag films. These nanostructures can support hotspots in air or solution.

Hierarchical micro- and nanostructures represent a new type of PERS-active substrate[29,31,88,93,134,135]. By means of subwavelength and/or deep-subwavelength electromagnetic coupling, hierarchical structures could effectively bridge the gap between the several-wavelength scale in the far field and the several-nanometre scale of the hotspots in the near field. In particular, it is necessary to develop hierarchical structures for plasmon-enhanced spectroscopies working in infrared regions in which the gap between the length scales is one to two orders of magnitude larger than that in the UV and visible regions. It is possible that hierarchical photonic–plasmonic devices could be designed to imbue TERS with far greater versatility. To fabricate new multiscale plasmonic materials, it is essential to understand the mechanism of the multiscale electromagnetic coupling.

To maximize the local electromagnetic field, it is possible to design nanostructures that support plasmonic Fano-resonance or double resonance due to near-field or far-field electromagnetic interference between nanostructures[35,136]. Some Fano-resonance nanostructures are well suited for PERS applications because they significantly enhance the local electromagnetic field at one wavelength and enhance the emission efficiency at another wavelength[137–139]. The Fano-resonance effect can also be extended to electromagnetic coupling between plasmonic nanostructures and probe materials in plasmon-enhanced infrared spectroscopy. Recently, the plasmon resonance of graphene nanoribbon arrays was dynamically tuned by the applied voltage to selectively probe a protein at different vibrational frequencies. A very sensitive overlap between the plasmon band and the vibrational bands of protein molecules produces extinction spectra with a significant Fano-type line shape[140].

The shell-isolated strategy can improve the stability of nanoparticles and target systems if the ultrathin shell materials are chemically stable and inert. However, the commonly used SiO_2 dissolves in alkaline media, which limits the applications of SHINERS. Besides, the shell SiO_2 is typically porous, which restricts the large-scale preparation of pinhole-free shell-isolated nanoparticles with shell thickness down to 2 nm. Therefore, it is highly desirable to develop other shell materials that can be easily prepared. It is now possible to develop ultrathin and compact Au@MnO_2 and Au@Ag_2S nanoparticles in alkaline systems[141,142]. The thinnest shell materials are 2D materials, such as graphene[143] and hexagonal boron nitride (h-BN), with which the SHINERS sensitivity could be further increased by one order of magnitude; however, it is highly challenging to avoid creating pinholes in these materials. Although the PERS activity of Ag@shell nanoparticles is typically one to two orders of magnitude larger than that of Au@shell nanoparticles, it is still challenging to prepare pinhole-free, shell-isolated Ag nanoparticles with shell thickness down to 2 nm (REF. 144). In addition, the shell-isolated strategy can also be extended to TERS by preparing a shell-isolated Au or Ag tip of a scanning probe microscope.

New materials for other spectroscopic methods. Beyond PERS, there are other plasmon-enhanced spectroscopies, such as plasmon-enhanced infrared absorption spectroscopy by means of mid-infrared plasmonic materials, tip-enhanced infrared or terahertz spectroscopies[145–148] by means of terahertz plasmonic materials, and surface- or tip-enhanced (resonance) Raman optical activity for the identification of chirality and absolute configuration of samples[149]. In addition, several plasmon-enhanced nonlinear spectroscopies (PE-NLS), such as plasmon-enhanced sum frequency generation[150–152], plasmon-enhanced coherent anti-Stokes Raman spectroscopy (CARS) and plasmon-enhanced femtosecond stimulated Raman spectroscopy, are very promising for materials analysis owing to their much higher temporal resolution than linear PERS.

To develop PE-NLS methods, it is necessary to design corresponding plasmonic nanomaterials and nanostructures. For example, surface-enhanced CARS has been used to achieve single-molecule detection on well-designed nanostructures with nanoquadrumer discs[139]. The nanoquadrumer discs support three localized SPR peaks, which simultaneously match the three beams (two incident beams at different wavelengths and one anti-Stokes Raman-scattered beam) in CARS. In the development of plasmon-enhanced spectroscopy methods, research has focused on second-generation hotspots for trace-molecule detection. Further desirable developments would be to create third-generation PE-NLS hotspots that allow for energy and phase matching at the nanoscale, in order to improve the low enhancement effect that currently hinders these methods[153].

Owing largely to the tremendous progress made in the development of new plasmonic materials and nanostructures, we anticipate a growing number of applications of PERS in the near future, ranging from *in operando* characterization to the on-line inspection of materials processing.

1. Nalwa, H. S. *Handbook of Surfaces and Interfaces of Materials* VII–IX (Academic Press, 2001).
2. Politis, C., Meletis, E. I. & Schommers, W. Welcome to the *Journal of Surfaces and Interfaces of Materials*. *J. Surf. Interfaces Mater.* **1**, 1–3 (2013).
3. Fleischmann, M., Hendra, P. J. & McQuillan, A. J. Raman spectra of pyridine adsorbed at a silver electrode. *Chem. Phys. Lett.* **26**, 163–166 (1974).
First report of surface-enhanced Raman spectra.
4. Jeanmaire, D. L. & Van Duyne, R. P. Surface Raman spectroelectrochemistry. Part I. Heterocyclic, aromatic, and aliphatic amines adsorbed on the anodized silver electrode. *J. Electroanal. Chem.* **84**, 1–20 (1977).
Demonstration that the anomalous enhancement in surface Raman spectra is due to a new effect: the SERS effect.
5. Albrecht, M. G. & Creighton, J. A. Anomalously intense Raman spectra of pyridine at a silver electrode. *J. Am. Chem. Soc.* **99**, 5215–5217 (1977).
6. Nie, S. & Emory, S. R. Probing single molecules and single nanoparticles by surface-enhanced Raman scattering. *Science* **275**, 1102–1106 (1997).
7. Kneipp, K. *et al.* Single molecule detection using surface-enhanced Raman scattering (SERS). *Phys. Rev. Lett.* **78**, 1667–1670 (1997).
References 6 and 7 are the first two papers on single-molecule SERS.
8. Ding, S. Y., Zhang, X. M., Ren, B. & Tian, Z. Q. in *Encyclopedia of Analytical Chemistry* (ed. Meyers, R. A.) (Wiley, 2013).
9. Moskovits, M. Surface roughness and the enhanced intensity of Raman scattering by molecules adsorbed on metals. *J. Chem. Phys.* **69**, 4159–4161 (1978).
Giant Raman intensity demonstrated from a roughened Ag electrode was shown to originate from the excitation of surface plasmons.
10. Creighton, J. A., Blatchford, C. G. & Albrecht, M. G. Plasma resonance enhancement of Raman scattering by pyridine adsorbed on silver or gold sol particles of size comparable to the excitation wavelength. *J. Chem. Soc. Faraday Trans. 2* **75**, 790–798 (1979).
First experimental evidence that the SERS enhancement factor effect can be observed on Ag and Au colloids (nanoparticles).
11. Stöckle, R. M., Suh, Y. D., Deckert, V. & Zenobi, R. Nanoscale chemical analysis by tip-enhanced Raman spectroscopy. *Chem. Phys. Lett.* **318**, 131–136 (2000).
12. Anderson, M. S. Locally enhanced Raman spectroscopy with an atomic force microscope. *Appl. Phys. Lett.* **76**, 3130–3132 (2000).
13. Hayazawa, N., Inouye, Y., Sekkat, Z. & Kawata, S. Metallized tip amplification of near-field Raman scattering. *Opt. Commun.* **183**, 333–336 (2000).
14. Pettinger, B., Picardi, G., Schuster, R. & Ertl, G. Surface enhanced Raman spectroscopy: towards single molecular spectroscopy. *Electrochemistry* **68**, 942–949 (2000).
References 11 to 14 are the first four papers reporting on TERS.
15. Li, J. F. *et al.* Shell-isolated nanoparticle-enhanced Raman spectroscopy. *Nature* **464**, 392–395 (2010).
The first paper on the invention of SHINERS.
16. Chase, D. B. & Parkinson, B. A. Surface-enhanced Raman spectroscopy in the near-infrared. *Appl. Spectrosc.* **42**, 1186–1187 (1988).
17. Ren, B. *et al.* Surface-enhanced Raman scattering in the ultraviolet spectral region: UV-SERS on rhodium and ruthenium electrodes. *J. Am. Chem. Soc.* **125**, 9598–9599 (2003).
18. Tian, Z. Q., Yang, Z. L., Ren, B. & Wu, D. Y. in *Surface-Enhanced Raman Scattering* (eds Kneipp, K., Moskovits, M. & Kneipp, H.) 125–146 (Springer, 2006).
19. Nie, S., Lipscomb, L. A. & Yu, N. T. Surface-enhanced hyper-Raman spectroscopy. *Appl. Spectrosc. Rev.* **26**, 203–276 (1991).
20. Liang, E. J., Weippert, A., Funk, J. M., Materny, A. & Kiefer, W. Experimental observation of surface-enhanced coherent anti-Stokes Raman scattering. *Chem. Phys. Lett.* **227**, 115–120 (1994).
21. Frontiera, R. R., Henry, A. I., Gruenke, N. L. & Van Duyne, R. P. Surface-enhanced femtosecond stimulated Raman spectroscopy. *J. Phys. Chem. Lett.* **2**, 1199–1203 (2011).
22. Wickramasinghe, H. K., Chaigneau, M., Yasukuni, R., Picardi, G. & Ossikovski, R. Billion-fold increase in tip-enhanced Raman signal. *ACS Nano* **8**, 3421–3426 (2014).
23. Aroca, R. F. Plasmon enhanced spectroscopy. *Phys. Chem. Chem. Phys.* **15**, 5355–5363 (2013).
24. Stiles, P. L., Dieringer, J. A., Shah, N. C. & Van Duyne, R. P. Surface-enhanced Raman spectroscopy. *Annu. Rev. Anal. Chem.* **1**, 601–626 (2008).
25. Liao, P. F. *et al.* Surface-enhanced Raman scattering from microlithographic silver particle surfaces. *Chem. Phys. Lett.* **82**, 355–359 (1981).
26. Tian, Z. Q., Ren, B., Li, J. F. & Yang, Z. L. Expanding generality of surface-enhanced Raman spectroscopy with borrowing SERS activity strategy. *Chem. Commun.* 3514–3534 (2007).
27. Freeman, R. G. *et al.* Self-assembled metal colloid monolayers: an approach to SERS substrates. *Science* **267**, 1629–1632 (1995).
28. Dick, L. A., McFarland, A. D., Haynes, C. L. & Van Duyne, R. P. Metal film over nanosphere (MFON) electrodes for surface-enhanced Raman spectroscopy (SERS): improvements in surface nanostructure stability and suppression of irreversible loss. *J. Phys. Chem. B* **106**, 853–860 (2002).
29. Greeneltch, N. G., Blaber, M. G., Henry, A. I., Schatz, G. C. & Van Duyne, R. P. Immobilized nanorod assemblies: fabrication and understanding of large area surface-enhanced Raman spectroscopy substrates. *Anal. Chem.* **85**, 2297–2303 (2013).
30. Li, W., Camargo, P. H. C., Lu, X. & Xia, Y. Dimers of silver nanospheres: facile synthesis and their use as hot spots for surface-enhanced Raman scattering. *Nano Lett.* **9**, 485–490 (2009).

31. Zhang, X. *et al.* Hierarchical porous plasmonic metamaterials for reproducible ultrasensitive surface-enhanced Raman spectroscopy. *Adv. Mater.* **27**, 1090–1096 (2015).
32. McMahon, J. M. *et al.* Correlating the structure, optical spectra, and electrodynamics of single silver nanocubes. *J. Phys. Chem. C* **113**, 2731–2735 (2009).
33. Wustholz, K. L. *et al.* Structure–activity relationships in gold nanoparticle dimers and trimers for surface-enhanced Raman spectroscopy. *J. Am. Chem. Soc.* **132**, 10903–10910 (2010).
34. Shegai, T. *et al.* Managing light polarization via plasmon–molecule interactions within an asymmetric metal nanoparticle trimer. *Proc. Natl Acad. Sci. USA* **105**, 16448–16453 (2008).
35. Gallinet, B., Siegfried, T., Sigg, H., Nordlander, P. & Martin, O. J. F. Plasmonic radiance: probing structure at the Ångström scale with visible light. *Nano Lett.* **13**, 497–503 (2013).
36. Doering, W. E., Piotti, M. E., Natan, M. J. & Freeman, R. G. SERS as a foundation for nanoscale, optically detected biological labels. *Adv. Mater.* **19**, 3100–3108 (2007).
37. Anker, J. N. *et al.* Biosensing with plasmonic nanosensors. *Nat. Mater.* **7**, 442–453 (2008).
38. Tian, Z. Q. & Ren, B. Adsorption and reaction at electrochemical interfaces as probed by surface-enhanced Raman spectroscopy. *Annu. Rev. Phys. Chem.* **55**, 197–229 (2004).
39. Wu, D. Y., Li, J. F., Ren, B. & Tian, Z. Q. Electrochemical surface-enhanced Raman spectroscopy of nanostructures. *Chem. Soc. Rev.* **37**, 1025–1041 (2008).
40. McAughtrie, S., Faulds, K. & Graham, D. Surface enhanced Raman spectroscopy (SERS): potential applications for disease detection and treatment. *J. Photochem. Photobiol. C* **21**, 40–53 (2014).
41. Gao, P. & Weaver, M. J. Surface-enhanced Raman spectroscopy as a probe of adsorbate-surface bonding: benzene and monosubstituted benzenes adsorbed at gold electrodes. *J. Phys. Chem.* **89**, 5040–5046 (1985).
42. Fleischmann, M., Tian, Z. Q. & Li, L. J. Raman spectroscopy of adsorbates on thin film electrodes deposited on silver substrates. *J. Electroanal. Chem.* **217**, 397–410 (1987).
43. Aramaki, K., Kiuchi, T., Sumiyoshi, T. & Nishihara, H. Surface enhanced Raman scattering and impedance studies on the inhibition of copper corrosion in sulphate solutions by 5-substituted benzotriazoles. *Corros. Sci.* **32**, 593–607 (1991).
44. Zou, S. & Weaver, M. J. Surface-enhanced Raman scattering on uniform transition-metal films: toward a versatile adsorbate vibrational strategy for solid-nonvacuum interfaces? *Anal. Chem.* **70**, 2387–2395 (1998).
45. Pettinger, B., Schambach, P., Villagómez, C. J. & Scott, N. Tip-enhanced Raman spectroscopy: near-fields acting on a few molecules. *Annu. Rev. Phys. Chem.* **63**, 379–399 (2012).
An excellent review on TERS from its history and principles to applications.
46. Schmid, T., Opilik, L., Blum, C. & Zenobi, R. Nanoscale chemical imaging using tip-enhanced Raman spectroscopy: a critical review. *Angew. Chem. Int. Ed. Engl.* **52**, 5940–5954 (2013).
47. Anema, J. R., Li, J. F., Yang, Z. L., Ren, B. & Tian, Z. Q. Shell-isolated nanoparticle-enhanced Raman spectroscopy: expanding the versatility of surface-enhanced Raman scattering. *Annu. Rev. Anal. Chem.* **4**, 129–150 (2011).
48. Li, X. *et al.* High-temperature surface enhanced Raman spectroscopy for *in situ* study of solid oxide fuel cell materials. *Energy Environ. Sci.* **7**, 306–310 (2014).
49. Hy, S. *et al. In situ* surface enhanced Raman spectroscopic studies of solid electrolyte interphase formation in lithium ion battery electrodes. *J. Power Sources* **256**, 324–328 (2014).
50. Hy, S., Felix, F., Rick, J., Su, W. N. & Hwang, B. J. Direct *in situ* observation of Li_2O evolution on Li-rich high-capacity cathode material, $Li[Ni_xLi_{(1-2x)/3}Mn_{(2-x)/3}]O_2$ ($0 \le x \le 0.5$). *J. Am. Chem. Soc.* **136**, 999–1007 (2014).
51. Li, C. Y. *et al. In situ* monitoring of electrooxidation processes at gold single crystal surfaces using shell-isolated nanoparticle-enhanced Raman spectroscopy. *J. Am. Chem. Soc.* **137**, 7648–7651 (2015).
52. Stadler, J., Schmid, T. & Zenobi, R. Nanoscale chemical imaging of single-layer graphene. *ACS Nano* **5**, 8442–8448 (2011).
53. Chen, C., Hayazawa, N. & Kawata, S. A. 1.7 nm resolution chemical analysis of carbon nanotubes by tip-enhanced Raman imaging in the ambient. *Nat. Commun.* **5**, 3312 (2014).
54. Cao, Y. C., Jin, R. & Mirkin, C. A. Nanoparticles with Raman spectroscopic fingerprints for DNA and RNA detection. *Science* **297**, 1536–1540 (2002).
55. Chang, R. K. & Furtak, T. E. (eds) *Surface Enhanced Raman Scattering* (Plenum, 1982).
56. Moskovits, M. Surface-enhanced spectroscopy. *Rev. Mod. Phys.* **57**, 783 (1985).
57. Otto, A., Mrozek, I., Grabhorn, H. & Akemann, W. Surface-enhanced Raman scattering. *J. Phys.: Condens. Matter* **4**, 1143–1212 (1992).
58. Moskovits, M. Surface-enhanced Raman spectroscopy: a brief retrospective. *J. Raman Spectrosc.* **36**, 485–496 (2005).
59. Le Ru, E. C. & Etchegoin, P. G. Single-molecule surface-enhanced Raman spectroscopy. *Annu. Rev. Phys. Chem.* **63**, 65–87 (2012).
60. Schlücker, S. Surface-enhanced Raman spectroscopy: concepts and chemical applications. *Angew. Chem. Int. Ed. Engl.* **53**, 4756–4795 (2014).
61. Aravind, P. K., Nitzan, A. & Metiu, H. The interaction between electromagnetic resonances and its role in spectroscopic studies of molecules adsorbed on colloidal particles or metal spheres. *Surf. Sci.* **110**, 189–204 (1981).
62. Aravind, P. K. & Metiu, H. The effects of the interaction between resonances in the electromagnetic response of a sphere-plane structure; applications to surface enhanced spectroscopy. *Surf. Sci.* **124**, 506–528 (1983).
References 61 and 62 are the first two studies in which the electromagnetic coupling in a particle dimer system and in a particle-on-metal substrate system were reported.
63. Shalaev, V. M. & Sarychev, A. K. Nonlinear optics of random metal–dielectric films. *Phys. Rev. B* **57**, 13265–13288 (1998).
64. Le Ru, E. C., Etchegoin, P. G. & Meyer, M. Enhancement factor distribution around a single surface-enhanced Raman scattering hot spot and its relation to single molecule detection. *J. Chem. Phys.* **125**, 204701–204713 (2006).
65. Kleinman, S. L., Frontiera, R. R., Henry, A. I., Dieringer, J. A. & Van Duyne, R. P. Creating, characterizing, and controlling chemistry with SERS hot spots. *Phys. Chem. Chem. Phys.* **15**, 21–36 (2013).
66. McMahon, J. M., Li, S., Ausman, L. K. & Schatz, G. C. Modeling the effect of small gaps in surface-enhanced Raman spectroscopy. *J. Phys. Chem. C* **116**, 1627–1637 (2012).
67. Moreau, A. *et al.* Controlled-reflectance surfaces with film-coupled colloidal nanoantennas. *Nature* **492**, 86–89 (2012).
68. Wei, H. & Xu, H. Hot spots in different metal nanostructures for plasmon-enhanced Raman spectroscopy. *Nanoscale* **5**, 10794–10805 (2013).
69. Shiohara, A., Wang, Y. & Liz-Marzán, L. M. Recent approaches toward creation of hot spots for SERS detection. *J. Photochem. Photobiol. C* **21**, 2–25 (2014).
70. Ding, S. Y., Yi, J., Li, J. F. & Tian, Z. Q. A theoretical and experimental approach to shell-isolated nanoparticle-enhanced Raman spectroscopy of single-crystal electrodes. *Surf. Sci.* **631**, 73–80 (2015).
71. Jiang, Bosnick, K., Maillard, M. & Brus, L. Single molecule Raman spectroscopy at the junctions of large Ag nanocrystals. *J. Phys. Chem. B* **107**, 9964–9972 (2003).
72. Sonntag, M. D. *et al.* Molecular plasmonics for nanoscale spectroscopy. *Chem. Soc. Rev.* **43**, 1230–1247 (2014).
73. Hao, E. & Schatz, G. C. Electromagnetic fields around silver nanoparticles and dimers. *J. Chem. Phys.* **120**, 357–366 (2004).
74. Cecchini, M. P., Turek, V. A., Paget, J., Kornyshev, A. A. & Edel, J. B. Self-assembled nanoparticle arrays for multiphase trace analyte detection. *Nat. Mater.* **12**, 165–171 (2013).
75. Banholzer, M. J., Millstone, J. E., Qin, L. & Mirkin, C. A. Rationally designed nanostructures for surface-enhanced Raman spectroscopy. *Chem. Soc. Rev.* **37**, 885–897 (2008).
76. Fang, Y., Seong, N. H. & Dlott, D. D. Measurement of the distribution of site enhancements in surface-enhanced Raman scattering. *Science* **321**, 388–392 (2008).
First experimental evidence for the contribution to the overall Raman signal from various sites on SERS substrates.
77. Yang, L., Li, P., Liu, H., Tang, X. & Liu, J. A dynamic surface enhanced Raman spectroscopy method for ultra-sensitive detection: from the wet state to the dry state. *Chem. Soc. Rev.* **44**, 2837–2848 (2015).
78. Camden, J. P. *et al.* Probing the structure of single-molecule surface-enhanced Raman scattering hot spots. *J. Am. Chem. Soc.* **130**, 12616–12617 (2008).
79. Chen, G. *et al.* High-purity separation of gold nanoparticle dimers and trimers. *J. Am. Chem. Soc.* **131**, 4218–4219 (2009).
80. Rycenga, M. *et al.* Generation of hot spots with silver nanocubes for single-molecule detection by surface-enhanced Raman scattering. *Angew. Chem. Int. Ed. Engl.* **50**, 5473–5477 (2011).
81. Lim, D. K., Jeon, K. S., Kim, H. M., Nam, J. M. & Suh, Y. D. Nanogap-engineerable Raman-active nanodumbbells for single-molecule detection. *Nat. Mater.* **9**, 60–67 (2010).
82. Thacker, V. V. *et al.* DNA origami based assembly of gold nanoparticle dimers for surface-enhanced Raman scattering. *Nat. Commun.* **5**, 3448 (2014).
83. Kleinman, S. L. *et al.* Single-molecule surface-enhanced Raman spectroscopy of crystal violet isotopologues: theory and experiment. *J. Am. Chem. Soc.* **133**, 4115–4122 (2011).
84. Chen, S. Y. & Lazarides, A. A. Quantitative amplification of Cy5 SERS in 'warm spots' created by plasmonic coupling in nanoparticle assemblies of controlled structure. *J. Phys. Chem. C* **113**, 12167–12175 (2009).
85. Gandra, N., Abbas, A., Tian, L. & Singamaneni, S. Plasmonic planet–satellite analogues: hierarchical self-assembly of gold nanostructures. *Nano Lett.* **12**, 2645–2651 (2012).
86. Wang, H., Levin, C. S. & Halas, N. J. Nanosphere arrays with controlled sub-10-nm gaps as surface-enhanced Raman spectroscopy substrates. *J. Am. Chem. Soc.* **127**, 14992–14993 (2005).
87. Peng, B. *et al.* Vertically aligned gold nanorod monolayer on arbitrary substrates: self-assembly and femtomolar detection of food contaminants. *ACS Nano* **7**, 5993–6000 (2013).
88. Tian, Z. Q. *et al.* Surface-enhanced Raman scattering from transition metals with special surface morphology and nanoparticle shape. *Faraday Discuss.* **132**, 159–170 (2006).
89. Bartlett, P. N., Baumberg, J. J., Coyle, S. & Abdelsalam, M. E. Optical properties of nanostructured metal films. *Faraday Discuss.* **125**, 117–132 (2004).
Demonstration of a new SERS substrate with nanovoid arrays.
90. Abdelsalam, M. E. *et al.* Electrochemical SERS at a structured gold surface. *Electrochem. Commun.* **7**, 740–744 (2005).
91. Tian, C., Deng, Y., Zhao, D. & Fang, J. Plasmonic silver supercrystals with ultrasmall nanogaps for ultrasensitive SERS-based molecule detection. *Adv. Opt. Mater.* **3**, 404–411 (2015).
92. Brown, R. J. C. & Milton, M. J. T. Nanostructures and nanostructured substrates for surface-enhanced Raman scattering (SERS). *J. Raman Spectrosc.* **39**, 1313–1326 (2008).
93. Huang, F. M. *et al.* Dressing plasmons in particle-in-cavity architectures. *Nano Lett.* **11**, 1221–1226 (2011).
94. Chen, S. Y. *et al.* Gold nanoparticles on polarizable surfaces as Raman scattering antennas. *ACS Nano* **4**, 6535–6546 (2010).
95. Li, A., Isaacs, S., Abdulhalim, I. & Li, S. Ultrahigh enhancement of electromagnetic fields by exciting localized with extended surface plasmons. *J. Phys. Chem. C* **119**, 19382–19389 (2015).
96. Tian, J. H. *et al.* Study of molecular junctions with a combined surface-enhanced Raman and mechanically controllable break junction method. *J. Am. Chem. Soc.* **128**, 14748–14749 (2006).
97. Qian, X. *et al. In vivo* tumor targeting and spectroscopic detection with surface-enhanced Raman nanoparticle tags. *Nat. Biotechnol.* **26**, 83–90 (2008).
98. Krafft, C. & Popp, J. The many facets of Raman spectroscopy for biomedical analysis. *Anal. Bioanal. Chem.* **407**, 699–717 (2015).
99. Mahajan, S., Richardson, J., Brown, T. & Bartlett, P. N. SERS-melting: a new method for discriminating mutations in DNA sequences. *J. Am. Chem. Soc.* **130**, 15589–15601 (2008).
100. Xu, L. J. *et al.* Label-free surface-enhanced Raman spectroscopy detection of DNA with single-base sensitivity. *J. Am. Chem. Soc.* **137**, 5149–5154 (2015).
101. Sherry, L. J. *et al.* Localized surface plasmon resonance spectroscopy of single silver nanocubes. *Nano Lett.* **5**, 2034–2038 (2005).

102. Zhang, S., Bao, K., Halas, N. J., Xu, H. & Nordlander, P. Substrate-induced Fano resonances of a plasmonic nanocube: a route to increased-sensitivity localized surface plasmon resonance sensors revealed. *Nano Lett.* **11**, 1657–1663 (2011).
103. Ciracì, C. *et al.* Probing the ultimate limits of plasmonic enhancement. *Science* **337**, 1072–1074 (2012).
104. Van Duyne, R. P. & Haushalter, J. P. Surface-enhanced Raman spectroscopy of adsorbates on semiconductor electrode surfaces: tris(bipyridine)ruthenium(II) adsorbed on silver-modified *n*-GaAs(100). *J. Phys. Chem.* **87**, 2999–3003 (1983).
105. Mubeen, S. *et al.* Plasmonic properties of gold nanoparticles separated from a gold mirror by an ultrathin oxide. *Nano Lett.* **12**, 2088–2094 (2012).
106. Mauser, N. & Hartschuh, A. Tip-enhanced near-field optical microscopy. *Chem. Soc. Rev.* **43**, 1248–1262 (2014).
107. Kumar, N., Mignuzzi, S., Su, W. & Roy, D. Tip-enhanced Raman spectroscopy: principles and applications. *EPJ Tech. Instrum.* **2**, 9 (2015).
108. Graham, D. The next generation of advanced spectroscopy: surface enhanced Raman scattering from metal nanoparticles. *Angew. Chem. Int. Ed. Engl.* **49**, 9325–9327 (2010).
109. Ge, J. J. *et al.* Rubbing-induced molecular reorientation on an alignment surface of an aromatic polyimide containing cyanobiphenyl side chains. *J. Am. Chem. Soc.* **123**, 5768–5776 (2001).
110. Taz, H. *et al. In situ* localized surface plasmon resonance (LSPR) spectroscopy to investigate kinetics of chemical bath deposition of CdS thin films. *J. Phys. Chem. C* **119**, 5033–5039 (2015).
111. Li, L., Steiner, U. & Mahajan, S. Single nanoparticle SERS probes of ion intercalation in metal-oxide electrodes. *Nano Lett.* **14**, 495–498 (2014).
112. Berweger, S. *et al.* Optical nanocrystallography with tip-enhanced phonon Raman spectroscopy. *Nat. Nanotechnol.* **4**, 496–499 (2009).
113. Rodriguez, R. D. *et al.* Surface- and tip-enhanced Raman spectroscopy reveals spin-waves in iron oxide nanoparticles. *Nanoscale* **7**, 9545–9551 (2015).
114. Zhang, R. *et al.* Chemical mapping of a single molecule by plasmon-enhanced Raman scattering. *Nature* **498**, 82–86 (2013).
Resolution of TERS shown to be increased to the sub-nanometre under ultrahigh vacuum and at low temperature.
115. Barbry, M. *et al.* Atomistic near-field nanoplasmonics: reaching atomic-scale resolution in nano-optics. *Nano Lett.* **15**, 3410–3419 (2015).
116. Duan, S. *et al.* Theoretical modeling of plasmon-enhanced Raman images of a single molecule with subnanometer resolution. *J. Am. Chem. Soc.* **137**, 9515–9518 (2015).
117. Zhang, C., Chen, B. Q. & Li, Z. Y. Optical origin of subnanometer resolution in tip-enhanced Raman mapping. *J. Phys. Chem. C* **119**, 11858–11871 (2015).
118. Liu, Z. *et al.* Revealing the molecular structure of single-molecule junctions in different conductance states by fishing-mode tip-enhanced Raman spectroscopy. *Nat. Commun.* **2**, 305 (2011).
119. Deckert-Gaudig, T., Kämmer, E. & Deckert, V. Tracking of nanoscale structural variations on a single amyloid fibril with tip-enhanced Raman scattering. *J. Biophotonics* **5**, 215–219 (2012).
120. Zeng, Z. C. *et al.* Electrochemical tip-enhanced Raman spectroscopy. *J. Am. Chem. Soc.* **137**, 11928–11931 (2015).
121. Honesty, N. R. & Gewirth, A. A. Shell-isolated nanoparticle enhanced Raman spectroscopy (SHINERS) investigation of benzotriazole film formation on Cu(100), Cu(111), and Cu(poly). *J. Raman Spectrosc.* **43**, 46–50 (2012).
122. Wang, H., Jiang, X., Lee, S. T. & He, Y. Silicon nanohybrid-based surface-enhanced Raman scattering sensors. *Small* **10**, 4455–4468 (2014).
123. Naik, G. V., Shalaev, V. M. & Boltasseva, A. Alternative plasmonic materials: beyond gold and silver. *Adv. Mater.* **25**, 3264–3294 (2013).
124. Murray, W. A. & Barnes, W. L. Plasmonic materials. *Adv. Mater.* **19**, 3771–3782 (2007).
125. Blaber, M. G., Arnold, M. D. & Ford, M. J. Optical properties of intermetallic compounds from first principles calculations: a search for the ideal plasmonic material. *J. Phys.: Condens. Matter* **21**, 144211 (2009).
126. Boltasseva, A. & Atwater, H. A. Low-loss plasmonic metamaterials. *Science* **331**, 290–291 (2011).
127. Luther, J. M., Jain, P. K., Ewers, T. & Alivisatos, A. P. Localized surface plasmon resonances arising from free carriers in doped quantum dots. *Nat. Mater.* **10**, 361–366 (2011).
128. McMahon, J. M., Schatz, G. C. & Gray, S. K. Plasmonics in the ultraviolet with the poor metals Al, Ga, In, Sn, Tl, Pb, and Bi. *Phys. Chem. Chem. Phys.* **15**, 5415–5423 (2013).
129. Zhong, Y., Malagari, S. D., Hamilton, T. & Wasserman, D. Review of mid-infrared plasmonic materials. *J. Nanophotonics* **9**, 093791 (2015).
130. Grigorenko, A. N., Polini, M. & Novoselov, K. S. Graphene plasmonics. *Nat. Photonics* **6**, 749–758 (2012).
131. Hanham, S. M. & Maier, S. A. in *Active Plasmonics and Tuneable Plasmonic Metamaterials* (eds Zayats, A. V. & Maier, S.) 243–260 (Wiley, 2013).
132. Zhang, H., Jin, M. & Xia, Y. Noble-metal nanocrystals with concave surfaces: synthesis and applications. *Angew. Chem. Int. Ed. Engl.* **51**, 7656–7673 (2012).
133. Zhang, Q., Large, N. & Wang, H. Gold nanoparticles with tipped surface structures as substrates for single-particle surface-enhanced Raman spectroscopy: concave nanocubes, nanotrisoctahedra, and nanostars. *ACS Appl. Mater. Interfaces* **6**, 17255–17267 (2014).
134. Zhang, Q., Lee, Y. H., Phang, I. Y., Lee, C. K. & Ling, X. Y. Hierarchical 3D SERS substrates fabricated by integrating photolithographic microstructures and self-assembly of silver nanoparticles. *Small* **10**, 2703–2711 (2014).
135. Ahmed, A. & Gordon, R. Single molecule directivity enhanced Raman scattering using nanoantennas. *Nano Lett.* **12**, 2625–2630 (2012).
136. Luk'yanchuk, B. *et al.* The Fano resonance in plasmonic nanostructures and metamaterials. *Nat. Mater.* **9**, 707–715 (2010).
137. Chu, Y., Wang, D., Zhu, W. & Crozier, K. B. Double resonance surface enhanced Raman scattering substrates: an intuitive coupled oscillator model. *Opt. Express* **19**, 14919–14928 (2011).
138. Ye, J. *et al.* Plasmonic nanoclusters: near field properties of the Fano resonance interrogated with SERS. *Nano Lett.* **12**, 1660–1667 (2012).
139. Zhang, Y. *et al.* Coherent anti-Stokes Raman scattering with single-molecule sensitivity using a plasmonic Fano resonance. *Nat. Commun.* **5**, 4424 (2014).
Single-molecule CARS performed on well-designed single nanoquadrumer discs.
140. Rodrigo, D. *et al.* Mid-infrared plasmonic biosensing with graphene. *Science* **349**, 165–168 (2015).
141. Lin, X. D. *et al.* Synthesis of ultrathin and compact Au@MnO_2 nanoparticles for shell-isolated nanoparticle-enhanced Raman spectroscopy (SHINERS). *J. Raman Spectrosc.* **43**, 40–45 (2012).
142. Li, J. F., Anema, J. R., Wandlowski, T. & Tian, Z. Q. Dielectric shell isolated and graphene shell isolated nanoparticle enhanced Raman spectroscopies and their applications. *Chem. Soc. Rev.* **44**, 8399–8409 (2015).
143. Bian, X. *et al.* Fabrication of graphene-isolated-Au-nanocrystal nanostructures for multimodal cell imaging and photothermal-enhanced chemotherapy. *Sci. Rep.* **4**, 6093 (2014).
144. Li, C. Y. *et al.* "Smart" Ag nanostructures for plasmon-enhanced spectroscopies. *J. Am. Chem. Soc.* **137**, 13784–13787 (2015).
145. Wu, C. *et al.* Fano-resonant asymmetric metamaterials for ultrasensitive spectroscopy and identification of molecular monolayers. *Nat. Mater.* **11**, 69–75 (2012).
146. Stanley, R. Plasmonics in the mid-infrared. *Nat. Photonics* **6**, 409–411 (2012).
147. Amenabar, I. *et al.* Structural analysis and mapping of individual protein complexes by infrared nanospectroscopy. *Nat. Commun.* **4**, 2890 (2013).
148. Wagner, M. *et al.* Ultrafast dynamics of surface plasmons in InAs by time-resolved infrared nanospectroscopy. *Nano Lett.* **14**, 4529–4534 (2014).
149. Ostovar pour, S. *et al.* Through-space transfer of chiral information mediated by a plasmonic nanomaterial. *Nat. Chem.* **7**, 591–596 (2015).
150. Baldelli, S., Eppler, A. S., Anderson, E., Shen, Y. R. & Somorjai, G. A. Surface enhanced sum frequency generation of carbon monoxide adsorbed on platinum nanoparticle arrays. *J. Chem. Phys.* **113**, 5432–5438 (2000).
151. Franck, V. & Abderrahmane, T. Sum-frequency generation spectroscopy of interfaces. *Rep. Prog. Phys.* **68**, 1095–1127 (2005).
152. Liu, W. T. & Shen, Y. R. *In situ* sum-frequency vibrational spectroscopy of electrochemical interfaces with surface plasmon resonance. *Proc. Natl Acad. Sci. USA* **111**, 1293–1297 (2014).
153. Hua, X. *et al.* Nature of surface-enhanced coherent Raman scattering. *Phys. Rev. A* **89**, 043841 (2014).
154. Raether, H. *Surface Plasmons on Smooth and Rough Surfaces and on Gratings* (Springer, 1988).
155. Willets, K. A. & Van Duyne, R. P. Localized surface plasmon resonance spectroscopy and sensing. *Annu. Rev. Phys. Chem.* **58**, 267–297 (2007).
156. Maier, S. A., Brongersma, M. L., Meltzer, P. G. K. S., Requicha, A. A. G. & Atwater, H. A. Plasmonics: a route to nanoscale optical devices. *Adv. Mater.* **13**, 1501–1505 (2001).
157. Brongersma, M. L. & Shalaev, V. M. The case for plasmonics. *Science* **328**, 440–441 (2010).
158. Atwater, H. A. & Polman, A. Plasmonics for improved photovoltaic devices. *Nat. Mater.* **9**, 205–213 (2010).
159. Brongersma, M. L., Halas, N. J. & Nordlander, P. Plasmon-induced hot carrier science and technology. *Nat. Nanotechnol.* **10**, 25–34 (2015).
160. Meng, L., Yam, C., Zhang, Y., Wang, R. & Chen, G. Multiscale modeling of plasmon-enhanced power conversion efficiency in nanostructured solar cells. *J. Phys. Chem. Lett.* **6**, 4410–4416 (2015).
161. Yamamoto, Y. S., Ozaki, Y. & Itoh, T. Recent progress and frontiers in the electromagnetic mechanism of surface-enhanced Raman scattering. *J. Photochem. Photobio. C* **21**, 81–104 (2014).
162. Kerker, M., Wang, D. S. & Chew, H. Surface enhanced Raman scattering (SERS) by molecules adsorbed at spherical particles: errata. *Appl. Opt.* **19**, 4159–4174 (1980).
163. Le Ru, E. C. & Etchegoin, P. G. Rigorous justification of the $|E|^4$ enhancement factor in surface enhanced Raman spectroscopy. *Chem. Phys. Lett.* **423**, 63–66 (2006).
164. Yoshida, K.i. *et al.* Quantitative evaluation of electromagnetic enhancement in surface-enhanced resonance Raman scattering from plasmonic properties and morphologies of individual Ag nanostructures. *Phys. Rev. B* **81**, 115406 (2010).
165. Le Ru, E. C. & Etchegoin, P. G. *Principles of Surface-Enhanced Raman Spectroscopy and Related Plasmonic Effects* (Elsevier, 2009).
An excellent book on SERS, hotspots and localized surface plasmon resonance.
166. Xu, H., Bjerneld, E. J., Käll, M. & Börjesson, L. Spectroscopy of single hemoglobin molecules by surface enhanced Raman scattering. *Phys. Rev. Lett.* **83**, 4357 (1999).
Demonstration of the importance of nanogaps in single-molecule SERS by electromagnetic computations and experiments.
167. Michaels, A. M., Nirmal, M. & Brus, L. E. Surface enhanced Raman spectroscopy of individual rhodamine 6G molecules on large Ag nanocrystals. *J. Am. Chem. Soc.* **121**, 9932–9939 (1999).
168. Etchegoin, P. G. & Le Ru, E. C. A perspective on single molecule SERS: current status and future challenges. *Phys. Chem. Chem. Phys.* **10**, 6079–6089 (2008).
169. Dieringer, J. A. *et al.* Surface-enhanced Raman excitation spectroscopy of a single rhodamine 6G molecule. *J. Am. Chem. Soc.* **131**, 849–854 (2008).
170. McMahon, J. M., Gray, S. K. & Schatz, G. C. Fundamental behavior of electric field enhancements in the gaps between closely spaced nanostructures. *Phys. Rev. B* **83**, 115428 (2011).
171. Zhu, W. & Crozier, K. B. Quantum mechanical limit to plasmonic enhancement as observed by surface-enhanced Raman scattering. *Nat. Commun.* **5**, 5228 (2014).
172. Zuloaga, J., Prodan, E. & Nordlander, P. Quantum description of the plasmon resonances of a nanoparticle dimer. *Nano Lett.* **9**, 887–891 (2009).
173. Savage, K. J. *et al.* Revealing the quantum regime in tunnelling plasmonics. *Nature* **491**, 574–577 (2012).
174. Johnson, P. B. & Christy, R. W. Optical constants of the noble metals. *Phys. Rev. B* **6**, 4370 (1972).
175. Palik, E. D. *Handbook of Optical Constants of Solids* Vol. 1 (Academic, 1998).

Acknowledgements
This work is financially supported by the National Natural Science Foundation of China (91427304, 21533006, 21321062 and 21522508) and Ministry of Science and Technology (2015CB932300). The authors thank X-Y. Cao for the English editing of this manuscript.

Competing interests statement
The authors declare no competing interests.